Marko Mikkonen

Comparison of simulated ELF magnetic field dosimetry between in vivo and in vitro

School of Electrical Engineering

Thesis submitted for examination for the degree of Master of Science in Technology.

Espoo September 23, 2015

Thesis supervisor:

Prof. Mervi Paulasto-Kröckel

Thesis advisor:

M.Sc.(Tech.) Anna-Maria Bique

Aalto University
School of Electrical
Engineering

AALTO UNIVERSITY
SCHOOL OF ELECTRICAL ENGINEERING

ABSTRACT OF THE
MASTER'S THESIS

Author: Marko Mikkonen

Title: Comparison of simulated ELF magnetic field dosimetry between in vivo and in vitro

Date: September 23, 2015 Language: English Number of pages: 8+67

Department of Electrical Engineering and Automation

Professorship: Electronics Integration and Reliability Code: S-113

Supervisor: Prof. Mervi Paulasto-Kröckel

Advisor: M.Sc.(Tech.) Anna-Maria Bique

Previous experiments studying magnetic field dosimetry have exploited a plethora of magnetic field parameters in order to study the effects of external magnetic fields onto biological tissue. The uncoordinated use and insufficient reporting of the parameters has made it difficult to address the fundamental phenomena behind the interaction of external magnetic fields and biological tissue.

This thesis assesses the comparability of effects of different parameters and common test setups by FEM simulations with Comsol Multiphysics. For the simulations, two models of common cell culture dishes, namely Petri and 48-well dish, and a simplified cylindrical model of a leg were built. In order to enhance the accuracy of the modeled cell culture medium, the conductivity of five different cell culture media was measured. Simulations were run using continuous sinusoidal, triangular, square waves and a pulsed bone growth signal with different field amplitudes and orientations. Also the effect of square wave risetime, the amount of liquid on cell culture dishes and the heating caused by sinusoidal fields was studied.

The results of this thesis describe the differences in the effects of the tested signal parameters have on the induced electric current densities. Based on the simulation results, improvements for the ELF EMF experiments are suggested. Also analytic equations to solve induced current densities on sinusoidal, triangular and square waved magnetic field input on circular cell culture dish are presented. The results of this thesis are significant as the parameter choice can affect whether the induced current densities reach the endogenous range.

Keywords: ELF EMF, Comsol, parametric simulations, dosimetry, FEM, in vitro, in vivo, experimental design

AALTO-YLIOPISTO
SÄHKÖTEKNIIKAN KORKEAKOULU

DIPLOMITYÖN
TIIVISTELMÄ

Tekijä: Marko Mikkonen

Työn nimi: Simuloitujen erittäin maatalataajuisten magneettikenttien dosimetrian vertailu in vivo ja in vitro

Päivämäärä: September 23, 2015 Kieli: Englanti Sivumäärä: 8+67

Sähkötekniikan ja Automaation laitos

Professuuri: Elektroniikan Integrointi ja Luotettavuus Koodi: S-113

Työn valvoja: Prof. Mervi Paulasto-Kröckel

Työn ohjaaja: DI. Anna-Maria Bique

Aiemmat magneettikenttien kudosvaikutusten tutkimukset ovat hyödyntäneet hyvin suurta määrää erilaisia magneettikentän parametreja erilaisille koeasetelmille. Erilaisten parametrien käyttö sekä koeasetelmien puutteellinen raportointi ovat tehneet tutkimustulosten vertailun vaikeaksi ja hankaloittaneet magneettikenttien ja kudoksen vuorovaikutusmekanismien ymmärtämistä.

Tämä diplomityö arvioi eri parametrien vaikutusta ja tyypillisten koeasetelmien vertailukelpoisuutta Comsol Multiphysics -ohjelmistolla suoritetuilla elementtimenetelmä-simulaatioilla. Näitä simulaatioita varten mallinnettiin Petri-malja ja 48-kuoppalevy sekä yksinkertainen sylinterimäinen malli säärestä. Soluviljelyastia-mallien tarkkuuden parantamiseksi tässä diplomityössä mitattiin myös viiden soluviljelymedian sähkönjohtavuudet. Simulaatiot ajettiin käyttäen jatkuvaa sinusoidaalista, kolmiomaista ja kanttimaista aaltoa eri taajuuksilla ja amplitudeilla sekä pulssitettua Bone Growth -signaalia. Näiden parametrien lisäksi tutkittiin myös kantti aallon nousuajan sekä soluviljelymaljoilla olevan nesteen määrän vaikutusta indusoituneisiin virtoihin.

Tämän diplomityön tulokset kuvaavat eroavaisuuksia, joita testatut parametrit aiheuttavat indusoituneissa sähkövirroissa. Tulosten perusteella esitetään myös parannuksia in vitro-kokeisiin sekä kirjallisuutta hyödyntäen analyyttiset yhtälöt sinusoidaaliselle, kolmiomaiselle ja kanttimaiselle magneettikentälle käytettäväksi apuna in vitro kokeiden suunnittelussa. Diplomityön tulokset ovat merkittäviä, sillä parametrien valinta voi vaikuttaa siihen yltävätkö indusoidut virrat biologisten virtojen suuruusluokkaan.

Avainsanat: ELF EMF, Comsol, dosimetria, FEM, parametrinen simulointi, in vitro, in vivo, koesuunnittelu

Acknowledgements

This master's thesis was done in the Department of Electrical Engineering and Automation in Aalto University School of Electrical Engineering for the EILB group. I would like to thank my supervisor prof. Mervi Paulasto-Kröckel for giving me the opportunity to make this thesis and my instructor M. Sc (Tech) Anna-Maria Bique for the endless ideas on the topic as well as for the help and support during the process of this thesis.

I would also like to thank our EILB group for the support and specially Julius for all the tips and ideas on simulation work. Also D.Sc. (Tech.) Patrick Grahn from Comsol Oy gave me valuable advice on Comsol Multiphysics.

Finally, I would like to thank my family and friends for the support during my studies. And last but not least, Sini, thanks for the ideas and support, all the help with R and especially for getting my mind off my work.

Otaniemi, September 23, 2015

Marko Mikkonen

Contents

Abstract ii

Abstract (in Finnish) iii

Acknowledgements iv

Contents v

Symbols and abbreviations vii

1 Introduction 1

2 Theory 3
- 2.1 Electromagnetism . . . 3
  - 2.1.1 Maxwell's equations . . . 3
  - 2.1.2 Electromagnetic fields . . . 4
  - 2.1.3 Electromagnetic fields and matter . . . 5
  - 2.1.4 Electromagnetic fields in nature . . . 7
- 2.2 The cell . . . 8
  - 2.2.1 Basics . . . 8
  - 2.2.2 Signaling . . . 10
  - 2.2.3 Endogenous bioelectricity . . . 10

3 Electromagnetic Field Dosimetry 14
- 3.1 Dosimetric quantities . . . 14
- 3.2 Electromagnetic fields and biological tissue . . . 15
  - 3.2.1 Electromagnetic coupling to biological tissue . . . 15
  - 3.2.2 Biophysical effects of electromagnetic fields . . . 17
- 3.3 Dosimetry in vivo . . . 18
- 3.4 Dosimetry in vitro . . . 23
  - 3.4.1 Experimental work . . . 23
  - 3.4.2 Modeling . . . 24

4 Methods 26
- 4.1 Finite Element Method . . . 26
- 4.2 Models . . . 28
  - 4.2.1 Meshing . . . 30
- 4.3 Material parameters . . . 32
- 4.4 Simulations . . . 35
  - 4.4.1 Data . . . 38
- 4.5 Error sources . . . 40

5 Results **42**
5.1 Temporal behavior and maximal amplitudes 42
5.2 Spatial behavior and analytic equations 46
5.3 Orientation of the magnetic field 48
5.4 Volume of the cell culture medium 50
5.5 Thermal simulations 52

6 Discussion **53**

7 Conclusions **57**

References **58**

A List of simulations **64**

Symbols and abbreviations

Symbols

${}^{e}\mathbf{A}$	Vector A of element e
B	Magnetic Flux density
D	Electric Displacement
E	Electric field
f	Frequency
$\mathbf{f}$	Force vector
H	Magnetic Field
h	Planck's constant, $6.626 * 10^{-34}\ m^2kg/s$
h_{half}	Half height
I	Electric current
J	Electric current density
K	Kinetic energy
$\underline{\mathbf{K}}$	Element matrix
M	Magnetization
N	Shape function
P	Power
p	Polarization
R	Resistance
r	Radius
t	Time
U	Voltage
X	Primary unknown quantity
$\mathbf{x}$	Vector of unknown quantities
μ	Magnetic permeability
ϵ	Electric permittivity
ρ	Density
σ	Electric conductivity
χ_M	Magnetic susceptibility
χ_E	Electric susceptibility
π	3.14159

Operators

$\nabla \times \mathbf{A}$	Curl of vector A
$\nabla \cdot \mathbf{A}$	Divergence of vector A
$\frac{\partial}{\partial t}$	Partial derivate over t
$\mathbf{A} \times \mathbf{B}$	Cross product of vectors A and B
$\sum_i$	Sum over index i

Abbreviations

A	Ampere
AC	Alternating current
ATP	Adenosine triphosphate
AUC	Area Under The Curve
C	Specific heat
°C	Degrees Celsius
Cl^-	Chlorine ion
CT	Computer Tomography
DC	Direct current
ELF	Extremely Low Frequency
EM	Electromagnetic
EMF	Electromagnetic Field
FD	Finite difference
FDTD	Finite Difference Time Domain
FEM	Finite Element Method
G	Gauss, 0.0001 T
ht	Thermal simulation
Hz	Hertz
ICNIRP	International Commition of Non-Ionizing Radiation Protection
IEEE	Institute of Electrical Engineers
IF	Intermediate Frequency
K	Kelvin
k	Thermal conductivity
K^+	Kalium ion
mf	Magnetic field simulation
MRI	Magnetic Resonance Imaging
Na^+	Sodium ion
NO	Nitric Oxide
OCD	Obsessive Compulsive Disorder
PEMF	Pulsed Electromagnetic Field
pd	Power density
RMS	Root Mean Square
S	Siemens
s	Second
SA	Specific Absorption
SAR	Specific Absorption Rate
sin	Sinusoidal
sqr	Square waved
STUK	Finnish radiation and nuclear safety authority
T	Tesla
tri	Triangular
V	Volt

1 Introduction

Electromagnetic fields are strongly involved in our everyday lives: Visible light keeps the world alive, electricity runs the modern world and even the smallest units of life, cells, exhibit electricity in their functioning. Electromagnetic fields interact with matter and are known to cause heating in tissues and distort neural functions with high enough amplitudes and frequencies. Even electromagnetic fields with extremely low frequencies and low amplitudes have been found to have biological effects.

Electromagnetic dosimetry is a field of science studying the effects of electromagnetic exposure to biological tissues, how the two interact and how the induced fields are distributed in the tissue. Dosimetry is difficult to measure directly in vivo and therefore a multitude of physical, analytic and numeric models have been developed to create safety limits for exposure to electromagnetic radiation. Whereas dosimetric studies and in vivo models concentrate on creating limits to keep the population safe from harmful impact from everyday electric devices, in vitro experiments seek to quantify the cellular level effects of exposure to external magnetic fields.

The effects of exposure to electromagnetic fields have been studied in vitro using a plethora of different parameters in varying stimulation geometries resulting in conflicting results. In these experiments various frequencies, amplitudes, waveforms and orientations of external magnetic field have been used to stimulate cell culture dishes of different shapes containing various amounts of varyingly conductive cell culture medium. In addition, these homogeneous models are used to describe a heterogeneous system in vivo, without considering the differences of conductivities or shapes between in vivo and in vitro. Even the shapes of the cells differ in vivo and in vitro, having most likely some effect on the fields induced. All these differences confound comparing results from different studies, and exposure in vivo and vitro.

This master's thesis aims to address the problems with parameter selection in extremely low frequency electromagnetic field experiments in vitro. This is accomplished by a series of Comsol Multiphysics simulations using models of a Petri dish, a 48-well dish and a simplified model of a leg and studying the fields induced by external magnetic field. The results of the simulations are used to achieve a better understanding on how different parameters effect the induced fields and how the induced fields compare to endogenous fields measured in cells. Conductivity measurement of the cell culture media used in the cell culture was also conducted as a part of this thesis, to ensure the representativeness of the in vitro models.

In the beginning of this thesis, physics of electromagnetic fields and basic of cell biology are presented as background on the subject. The chapter discussing cells also defines a biological range for endogenous electric fields and current densities. Chapter 3 discusses the concept of dosimetry and how it is studied in vivo and in vitro presenting also safety limits for electric and magnetic fields set by International Commission on Non-Ionizing Radiation Protection. Chapter 4 describes the methods,

models and simulations used for this thesis and elaborating also on the error sources in simulation work. Chapter 5 presents the results of the simulations work for this thesis, which are later analyzed in chapter 6, in order to describe how the results can be used to address the problems with ELF EMF parameter selection.

The results of this thesis aid in designing experiments in a controlled and reproducible way regarding the induced fields. The possibility to control the induced fields enables also the experimental validation of the main actor in the interaction between magnetic fields and tissue. In these ways the results of this thesis provide significant advancements for ELF EMF in vitro research.

2 Theory

Before addressing the dosimetry of electromagnetic fields, knowledge of the physics of electromagnetic fields (EMF) and the biology of the cells is needed. This chapter summarizes the basics of electromagnetism starting from the Maxwell's equations, discusses the different regions of the electromagnetic field spectrum and the interaction of external electromagnetic fields and matter. Also the electromagnetic fields in nature are briefly discussed to obtain context about the magnitudes of the electromagnetic fields surrounding us in everyday life.

As there are electrical phenomena also in living tissue, it is intuitive that external electromagnetic radiation is capable of affecting the functioning of cells and tissues. These effects and the study of them are discussed later in chapter 3. The end of this chapter describes the basics of cells, their signaling and electric activity in order to illustrate the complexity of cellular scale phenomena and different possibilities where external EMFs can affect cellular functions.

2.1 Electromagnetism

Electromagnetism studies the electromagnetic force, the most dominant and best known of the four basic forces [1, p. xii]. Classically, electromagnetism is described by fields surrounding charges: When another charge enters such a field, it experiences force. As all atoms contain charged particles, matter as well as biological tissue is affected by external electromagnetic fields. Therefore it is vital to understand the physics of electromagnetic fields, the vast spectrum of electromagnetic radiation and the interaction of the EMFs and matter in order to discuss the dosimetry.

2.1.1 Maxwell's equations

Electromagnetic fields are governed by Maxwell's equations, which can be stated in vector form in vacuum as follows [1, p. 326]:

$$\nabla \times \mathbf{E} = -\frac{\delta \mathbf{B}}{\delta t} \tag{1}$$

$$\nabla \times \mathbf{B} = -\frac{\delta(\mu_0 \epsilon_0 \mathbf{E})}{\delta t} + \mu_0 \mathbf{J} \tag{2}$$

$$\nabla \cdot \mathbf{E} = \frac{\rho}{\epsilon_0} \tag{3}$$

$$\nabla \cdot \mathbf{B} = 0 \tag{4}$$

where $\mathbf{B}$ is magnetic flux density, $\mathbf{E}$ is electric field, t is time, μ_0 is vacuum magnetic permeability, ϵ_0 vacuum electric permittivity and $\mathbf{J}$ current density. These four equations state that fields can arise either from charges or changing fields. The magnetic fields arise from changing electric fields or from magnetic charges, supposed they exist. In similar manner, the electric fields arise from electric charges or changing magnetic fields.

Individually, Faraday's law (equation 1) states that a changing magnetic field induces an equivalent changing electric field in a phenomenon known as electromagnetic induction. Equation 2 is known as the Ampere's law with Maxwell's correction. This equation states that a changing electric field creates an equivalent changing magnetic field. Gauss's law (equation 3) means essentially that the flux through any closed surface is a measure of the total charge within this surface [1, p. 67]. Equation 4 would describe the same effect for magnetic fields but since the existence of magnetic monopoles is not confirmed, the divergence of magnetic field equals to zero.

Magnetic flux density $\mathbf{B}$ used in description of Maxwell's equations is often used to describe the magnetic field instead of the magnetic field $\mathbf{H}$. These two parameters are related by:

$$\mathbf{B} = \mu_0(\mathbf{H} + \mathbf{M}) \tag{5}$$

Where $\mathbf{M}$ is the magnetization of the material in external magnetic field $\mathbf{H}$.

There is a similar, yet less frequently used flux term for electric fields called electric displacement $\mathbf{D}$, which can be written as

$$\mathbf{D} = \epsilon_0(\mathbf{E} + \mathbf{p}) \tag{6}$$

where $\mathbf{p}$ is the polarization of the material in external electric field $\mathbf{E}$.

2.1.2 Electromagnetic fields

As a phenomena, electromagnetic radiation is familiar to everyone. Our eyes are capable of perceiving photons in the frequency range of visible light, our cellphones communicate via radio frequencies and common x-ray exploits the tissue permeability of high frequency and high energy electromagnetic fields. The electromagnetic spectrum is shown in figure 1.

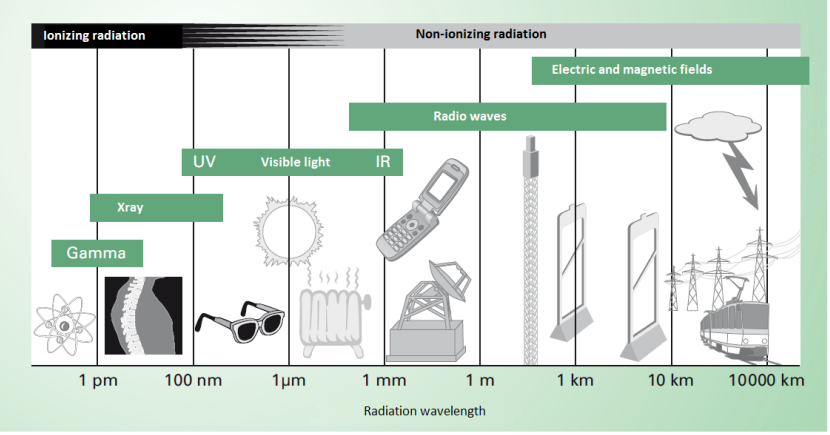

Figure 1: Spectrum of electromagnetic radiation. [2, p. 17: Modified]

Electromagnetic fields are carried by photons, which are elementary particles conveying the electromagnetic interaction. The electromagnetic spectrum can be divided into ionizing and non-ionizing radiation, depending on whether the photons have enough kinetic energy to ionize atoms or molecules. If the energy of the photon is more than 12 eV, the radiation can be considered ionizing [2, p.16]. By taking photoelectric effect (equation 7 [3, p. 364]) into account

$$K = hf \tag{7}$$

this energy can be stated to be approximately 3 PHz or 100 nm meaning that with lower frequencies or higher wavelengths the photons do not have enough energy to ionize atoms. This boundary lies roughly between UV and X-ray ranges of the electromagnetic spectrum. In equation 7, h is Planck's constant, f is the frequency of the radiation and K the kinetic energy of photons.

As seen in figure 1, simple electric and magnetic fields lie in the low frequency end of the spectrum ranging from static fields up to radio frequencies starting from 100 kHz. This low frequency range can be further divided into extremely low frequency (ELF, less than 300 Hz) and intermediate frequency (IF, 300 Hz - 100 kHz) range [2, p. 18,19] as shown in figure 2. The ranges presented here are not rigid and their definitions can vary.

Yet another noteworthy division within the spectrum with respect to relevance to dosimetric studies is that of quasi-static (< 30 MHz), resonance (30-3000 MHz) and surface-absorption (> 3000 MHz) ranges [2, p. 80]. In the quasi-static range below 30 MHz one can treat magnetic and electric fields separately without considerable error whereas in the other ranges this is not possible without notable error in the results. These domains are discussed in more detail at chapter 3.

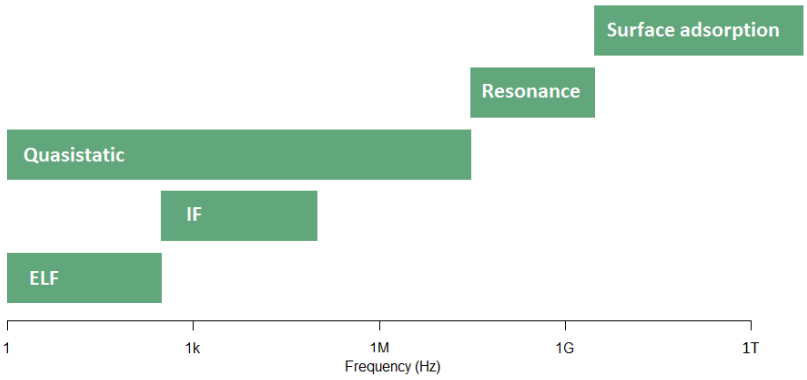

Figure 2: Lower end of the electromagnetic field spectrum.

2.1.3 Electromagnetic fields and matter

When placed into a changing magnetic field, an electric field is induced to the matter according to Faraday's Law (equation 1). This induced electric field causes further a

current density to the object as Ohm's law [1, p. 285] states:

$$J = \sigma E \tag{8}$$

where σ is material's electric conductivity. Since materials have some material-specific resistance to current flow, some of the energy is transformed into heat according to the Joule heating law [1, p. 290]:

$$P = UI = I^2R \tag{9}$$

where P is the power, U the voltage, I the electric current and R the resistance of the system.

As can be seen from the Maxwell's equations (1 - 4) and Ohm's law (8), magnetic permeability, electric permittivity and electric conductivity are significant in the coupling of materials and electromagnetic fields. These parameters are material specific and vary notably between different materials. Outside a vacuum the ϵ_0 and μ_0 are replaced by ϵ and μ, which relate to vacuum values according to equations

$$\epsilon = \epsilon_r \epsilon_0 \tag{10}$$

$$\mu = \mu_r \mu_0 \tag{11}$$

where subscript r denotes relative electric permittivity and relative magnetic permeability. Both the electric permittivity and magnetic permeability describe how much material is polarized or magnetized when placed in electric or magnetic field, respectively.

An external magnetic field causes reorientation of the magnetic dipoles occurring from electrons orbiting atomic nuclei. This is called magnetization, $\mathbf{M}$. When magnetization is parallel to the magnetic field, the material is said to be paramagnetic. If the magnetization opposes the external field, the material is diamagnetic. For these two material types, the magnetic dipoles return to random orientation as the materials are removed from the external magnetic field. There is also a third class of magnetization called ferromagnetism, where the magnetic dipoles arrange themselves also parallel to the external field. The difference between para- and ferromagnetic materials is, that ferromagnetic materials are capable of maintaining the magnetization also after the external field is removed. Iron is an example of a ferromagnetic material.

Magnetization is described as

$$\mathbf{M} = \chi_M \mathbf{H} \tag{12}$$

where χ_M is magnetic susceptibility of the material, which connects the magnetization of a material to the external magnetic field. As the magnetic flux density (equation 5) contains the magnetization term, it can be rewritten as

$$\mathbf{B} = \mu_0(1 + \chi_M)\mathbf{H} = \mu \mathbf{H} \tag{13}$$

so the relative permittivity can be linked to magnetic susceptibility:

$$\mu_r = 1 + \chi_M \tag{14}$$

In general, magnetism describes how a material is affected by an external magnetic field and vice versa. Diamagnetic materials have $\chi_M < 0$ and para- and ferromagnetic $\chi_M > 0$ meaning that diamagnetic materials are repelled by magnetic fields whereas paramagnetic and ferromagnetic materials are attracted by them. These effects are weak in dia- and paramagnetic materials compared to ferromagnets.

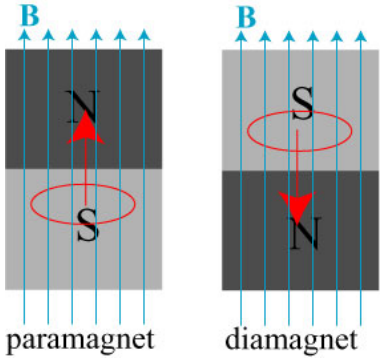

Figure 3: Dipole orientations of para- and diamagnetic materials in an external magnetic field [4]

In a similar way as a magnetic field aligns magnetic dipoles, an electric field aligns electric dipoles within a material. This phenomenon is called polarization. For linear dielectric materials within moderate electric fields, the polarization $\mathbf{p}$ can be written as

$$\mathbf{p} = \epsilon_0 \chi_E \mathbf{E} \tag{15}$$

where χ_E is the electric susceptibility of the material. As the electric displacement, equation 6, contains the polarization term, it can be rewritten as

$$\mathbf{D} = \epsilon_0(1 + \chi_E)\mathbf{E} = \epsilon \mathbf{E} \tag{16}$$

so the relative permittivity can be linked to electric susceptibility by

$$\epsilon_r = 1 + \chi_E \tag{17}$$

2.1.4 Electromagnetic fields in nature

Naturally occurring electromagnetic fields are usually very small compared to the fields created by artificial sources. In large scale, background magnetic fields on Earth are a summation of static geomagnetic field of 25 - 60 μT [2, p. 363] and a small high frequency field arising from currents in the ionosphere. The geomagnetic field depends on the distance from the poles, the lowest fields being near the equator. There is also a static electric field of 100-130 V/m [2, p. 364] between the earth's crust and ionosphere, which is maintained by ongoing thunderstorms around the globe. Locally within a thunderstorm, electric fields can be tens of kV/m. In lightnings, most powerful components of the EM spectrum last approximately 50 ms in the frequency range of 5-10 kHz [2, p. 366].

Aside from these global electromagnetic fields, there are also electric phenomena in living organisms and cells. Cells for example maintain an electric potential over their cellular membrane. This potential is called the resting membrane potential and it ranges from -50 mV to -100 mV usually being around -70 mV [5, p. 56]. These biological electromagnetic fields are discussed in more detail at the end of chapter 2.2.

2.2 The cell

Magnetic field dosimetry studied in this thesis, studies the effects of an external magnetic fields on biological tissue. To get an idea of how the induced fields can affect the cellular functions, one must understand the biology of a cell. Cells and tissues are complex systems directed by electrochemical signals that control both the cells and interactions between them. Cells have also been shown to respond to external magnetic fields.

This chapter aims to briefly introduce cellular biology, and present cellular phenomena that can be affected by external fields. More specifically, cellular signaling and endogenous bioelectricity are discussed. Based on the measured endogenous fields, biological ranges for endogenous electric fields and electric current densities are also established to be used as a baseline for interpreting the results of this thesis.

2.2.1 Basics

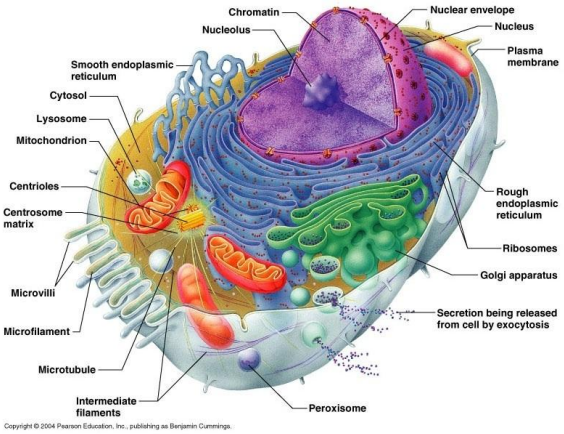

Figure 4: A typical eukaryotic cell. [6]

A cell can be defined to be the smallest autonomous unit of life. As such, it constitutes the basic structural and functional unit of multicellular organisms such as humans [5, p. 27]. Within the human body, there are about 10^{14} individual cells [5, p. 27] that can be divided into about 200 different types of specialized cells [7, p. 61] performing together to maintain body's homeostasis and in macroscopic level to create a functional individual. Human cells vary in size from 5 to 150

μm [5, p. 29] and the shape of the cells varies widely. A typical eukaryotic cell consists of a plasma membrane encapsulating the cytoplasm and nucleus as shown in Figure 4.

The cytoplasm consists of cytosol, ie. the intracellular fluid, and organelles of the cell. Cytosol is the fluid portion of cytoplasm comprising approximately 55% [7, p.76] of the cells volume. Cytosol contains mostly water, with various dissolved ions and molecules such as adenosine triphosphate (ATP) and proteins. The electric conductivity of cytosol is about 1 S/m [5, p. 45]. Organelles are structures specialized in performing different tasks in cellular functions. For example, mitochondria generate ATP through aerobic respiration [7, p. 85] and ribosomes are the sites of protein synthesis [7, p.80]. Within the cell is also the Nucleus, which is a spherical lipid bilayer covered structure that contains the chromosomes, the genetic information.

The plasma membrane consists of a lipid bilayer that creates a flexible yet strong barrier between the cytoplasm and extracellular matrix. Among the lipid molecules in the membrane there are a vast number of proteins. These proteins act as receptors, enzymes and antigens contributing to interaction between cells. Electrically, the plasma membrane behaves as capacitor, an insulator separating two conductors [5, p. 46]. Yet the membrane is not impermeable: Some small molecules like oxygen are able to freely diffuse through the membrane and embedded within the membrane. There are also protein-build channels and pumps that transfer larger molecules through the membrane. Ion channels enable the diffusion of larger molecules along their concentration gradient, whereas ion pumps use energy to move molecules against their concentration gradients [7, p. 68-72]. Arguably the most important ion pump is the sodium-potassium pump that transfers sodium and potassium ions with energy from the hydrolysis of ATP in order to maintain the membranes resting potential. An illustration of the cell membrane with ion channels and pumps is presented in figure 5.

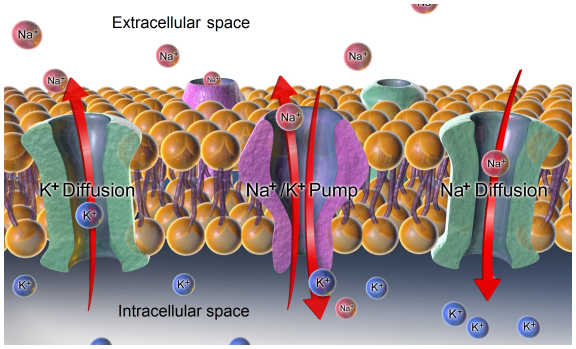

Figure 5: Na^+ and K^+ channels and pumps in cell membrane. [8]

Cells are surrounded by an extracellular matrix consisting of a complex polysaccharide and protein network secreted by the cells [9, G:13]. Alongside this secreted network, the extracellular space contains a solution of water and ions resembling a 0.9% solution of salt [5, p. 35], which has an electric conductivity of approximately 2 S/m [5, p. 45].

2.2.2 Signaling

In order to function properly, the cells in a multicellular organism such as a human need to communicate with each other. This is achieved by a fleet of extracellular signaling molecules and ions that function as chemical signals between cells facilitating cellular behavior. To be able to obtain a functional signaling system, a complex intracellular mechanisms are needed to control the amount and timing of the signaling molecules to ensure that the receiving cells interpret these signals correctly [9, p. 879]. The exact mechanisms of cellular signaling are beyond the scope of this thesis and are presented here very briefly. More detailed information on the topic can be found for example from chapter 15 of [9].

There are hundreds [9, p. 880] of different signaling molecules and ions that cells use for communication. These extend from macro molecules such as proteins and peptides to dissolved gases such as nitric oxide (NO). Some of the signaling molecules and ions, like Cl^- that controls the intracellular activity of many ions [10], are charged particles and therefore their release and movement results in flowing currents and thus electric fields. These endogenous electric fields play an important role in wound healing for example [11–13]. Endogenous electricity is discussed in more detail next chapter alongside other bioelectric phenomena.

Most of these molecules and ions are emitted from cells via exocytosis but some are also able to diffuse trough the plasma membrane and others stay on the plasma membrane and signal only upon cell-to-cell contact [9, p. 881]. These signaling molecules can act either locally or over longer distances to carry signals for example to the extremities of human body.

The signaling molecules attach to specific receptors on the plasma membrane of the target cell. This activates an intracellular signaling pathway leading to a reaction in the behavior of the target cell. The intracellular signaling pathway consists of a cascade of intracellular signal molecules that elicit a change to the cellular behavior. Depending on the signaling molecule and the state of the cell affected, the signals can for example affect the expression of genes, the metabolic pathways within the cell or the the shape of the cell via changes in the cytoskeleton.

2.2.3 Endogenous bioelectricity

As already mentioned earlier in chapter 2.1.4, the cells also exhibit inherent electrical phenomena. Cells are in fact electrical units surrounded and regulated by electric currents [14]. Animal cells maintain an electrochemical gradient over the plasma membrane maintained by active pumps and passive channels on the plasma membrane. This electric gradient is called the membrane potential and it ranges from -20 mV to -120 mV [9, p. 671], the inside of the plasma membrane being more negative than the outside. Often different proliferating cells and tumor cells exhibit lower membrane potentials than normal cells, the membrane potentials of muscle cells being among the highest potentials (< -90 mV) [15].

The membrane potential arises from the osmotic balance of ions across the plasma membrane, maintained mainly by passive K^+ leakage channels and active Na^+-K^+ -pumps. The leakage channels allow high permeability for K^+-ions [9, p.671] to diffuse along their electrochemical gradient. The Na^+-K^+ -pumps transfer 3 Na^+ ions out from the cell for every 2 K^+ ions they pump in thus maintaining the inner side of the cell more negative than the outside. The Cl^--ion equilibrium also contributes to the total membrane potential [9, p. 671]

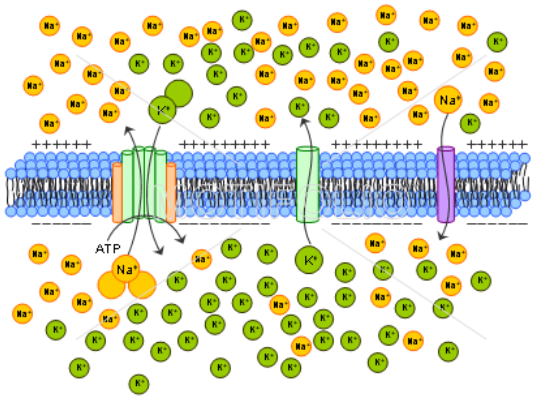

Figure 6: Active transportation of ions through the extracellular membrane creates the resting membrane potential. [16]

Most animal cells are passive and maintain the membrane potential for transportation purposes only, but there are also a few active cell types, namely neurons and muscle cells. These cells can be excited with an external stimulus to create an action potential, an electrical signal, capable of propagating on the plasma membrane due to voltage-gated ion channels that exist on the membranes [7, p. 140]. For example, transcranial magnetic stimulation (TMS) exploits short magnetic field pulses of up to 2.5 T to stimulate neurons in the brain non-invasively [17].

In neurons, the action potential is created when the membrane potential at the axon hillock of the neuron depolarizes above a threshold potential, usually about +20 mV from the resting membrane potential [5, p. 66]. The change in membrane potential at the axon hillock results in a spatial and temporal summation of signals from incoming synapses to the soma and the dendrites of the neuron [7, p. 445]. In skeletal muscle cells, an action potential is triggered when an action potential of a motor neuron synapsing to the muscle cell causes the release of neurotransmitter molecules to synaptic cleft that depolarizes the plasma membrane of the muscle cell and gives rise to an action potential [7, p. 315]. The smooth muscle cells in heart differ from skeletal muscles in being capable of transferring the action potential from one muscle cell to another via gap junctions [7, p. 327]. This enables the whole heart to contract once the contraction starts.

On top of the membrane potential, the electrical processes of surrounding cells

and the thermal movement of charged particles in cytosol and extracellular fluid generate an AC-noise field over the plasma membrane of a cell [2, p. 136]. The thermal noise field arises from the thermal movement of charged particles creating a fluctuating electric field producing approximately 3 μV transmembrane voltage. Other known types of noise in biological membranes are so called 1/f noise of about 10 μV arising from the ion current flows in ion channels and "shot" noise. The shot noise is generated when for example a voltage gated channel is opened and a larger number of ions rush in the cell as happens in the event of an action potential. Shot noise can be a major source of noise in cells. [18, p. 100]

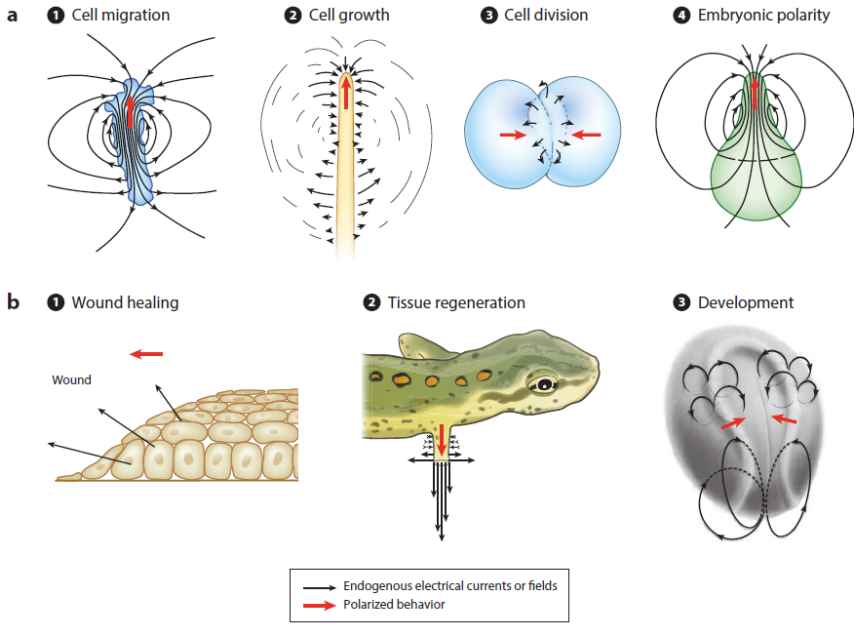

Figure 7: Electric currents surrounding cells and tissues. [14]

Aside from these well established electrical phenomena in cells, there are organized electric signals surrounding the cells and tissues within human body. Figure 13 displays some example cases of endogenous electric currents and fields. These electric currents rise from the polarized behavior in cells and tissues [14]. For electric current densities, trans-cellular currents of 1 mA/m^2 in migrating amoebas [14] and approximately 400 mA/m^2 at center of a wound in cell membrane [12] have been measured in single cells. In multicellular organisms electric currents have been measured for example during limb regeneration and other morphogenic rearrangements during vertebrate development [14]. Also wound potentials in epithelial tissue [13] are well established and for example currents degrading from initial 1 A/m^2 to 50 mA/m^2 level lasting several hours in bone fracture sites have been measured [11]. Based on these studies, the physiological range of endogenous electric current densities seems to lie within 1-1000 mA/m^2. For endogenous electric fields, Nuccitelli [11] has suggested a physiological range to be 0.01 - 2.0 V/m. The endogenous currents are likely to result from fluxes of different charged ions like calcium, potassium or

sodium, but currently little is known of the exact origins of these currents [14]. Table 1 summarizes some of the endogenous electric fields, electric currents and electric potentials measured.

	U(mV)	E(V/m)	J(mA/m2)
Membrane potential	-20 to -120	-2e6 to -12e6	-
Thermal noise	0.003	300	-
1/f noise	0.01	1000	-
Physiological range for endogenous fields	-	0.01 - 2.0	1 - 1000

Table 1: Electric potentials and electric fields within human body.

Endogenous currents have also been studied in vitro [19] using exogenous electric fields. This topic is addressed more specifically at chapter 3.4.

3 Electromagnetic Field Dosimetry

When a human body, or any other object, is placed within an external electromagnetic field, an electric field and a current density are induced according to Faraday's law. If the frequency of the radiation is high, the energy is directly absorbed by the tissue. Electromagnetic field dosimetry studies the effects of electromagnetic radiation on biological tissue. Below radio frequencies the biological effects of electromagnetic fields arise from induced electric fields and current densities whereas in higher frequency range the effects are mostly due to heating generated by EM-fields [2, p. 164]. These known effects require large enough an external field to occur. For small amplitude ELF EMF it is argued that the induced fields are not capable of eliciting biological effects [20] meaning that it is possible for these effects to be a product of the magnetic field itself.

This chapter discusses the EMF dosimetry starting from the common dosimetric quantities and interaction of the external EMFs and biological tissue for a view on how they interact and what affects the interaction. Then, dosimetry is assessed both in vivo and in vitro. In vivo dosimetry concentrates on creating safety limits to avoid direct harmful effects caused by EMFs whereas in vitro dosimetry studies more the effects of low amplitude EMFs on cells. Some of the safety limits are presented within this chapter to offer an idea of how they relate to the endogenous currents within tissues and the results of this thesis.

3.1 Dosimetric quantities

There are eight common physical quantities used to describe exposure to electromagnetic fields [2, p. 55]. Induced electric field **E** and the related induced current density **J** as well as magnetic field strength **H** and magnetic flux density **B** are used to measure the effects of external electromagnetic fields below 100 kHz. These parameters have been studied in more detail already in chapter 2.1. An object charged by external electric field is capable of discharging on contact. Therefore also contact current I_c describing such a discharge current is used as a dosimetric quantity.

At higher frequencies the Specific Absorption Rate (SAR, [W/kg]) is the most used quantity. It describes the ohmic absorption of power to lossy tissues via the electric field and current densities acting on it, ie. the absorption rate of energy into tissue per unit mass of the tissue. Local SAR can be described as [2, p. 48]

$$SAR = \frac{dP}{dm} = \frac{\sigma E_i^2}{\rho} \tag{18}$$

where P is the power, m the mass and ρ the density. Also the Specific Absorption (SA, [J/kg]) describing the energy per unit mass absorbed by the tissue and power density (pd, $[W/m^2]$) which describes the power of the electromagnetic waves perpendicular to the surface of the tissue are used to described electromagnetic field exposure

at high frequencies. The power density can be expressed as absolute value of the Poynting vector [2, p. 46], ie.

$$\mathbf{pd} = \mathbf{E} \times \mathbf{H} \tag{19}$$

The Specific absorption is most often used to describe pulsed microwave radiation.

3.2 Electromagnetic fields and biological tissue

The most important physical quantities for defining exposure to ELF EM fields are the electric field and current density induced by the external field. Below 100 kHz electromagnetic radiation couples to biological tissue via induction of electric field and current density and at higher frequencies by energy absorption, i.e. by heating. Especially neurons, muscle cells and some sensory receptors are susceptible to electrical stimulation [2, p. 164]. Therefore it is important to know how the EMFs interact with biological tissue in order to limit the exposure to external fields in order to avoid harmful effects to health.

3.2.1 Electromagnetic coupling to biological tissue

The primary material properties affecting the tissue coupling with electromagnetic fields are magnetic permeability μ, electric permittivity ϵ and electric conductivity σ. The magnetic permeability of biological tissue is very close to that of vacuum [21] and therefore the distortion of the external magnetic field caused by the tissue is negligible and can be disregarded without any considerable error. The electric permittivities of biological tissues on the other hand are noteworthy [22] and therefore tissues distort external electric fields strongly. Electric conductivities of biological tissues are rather low and therefore the magnetic field arising from induced currents, does not affect the external field notably [23, p. 24]. Under 1 MHz frequencies biological tissue can be considered to be a conductor, whereas at higher frequencies the behavior is better approximated as a lossy insulator [2, p. 63].

Tissue	χ_M	ϵ	σ (S/m)
Water	-1.298e-5 [24]	74.828 [25]	$0.055*10^{-6}$ [24]
Bone	$-8.86e^{-6}$ [21]	800 [22]	0.02 [22]
Muscle	$-9.05e^{-6*}$ [21]	$8e^{7}$ [22]	$\parallel$ 0.3 [22], $\perp$ 0.1 [22]
Skin	$-9.05e^{-6*}$ [21]	$1e^{5}$ [22]	$4e^{-4}$ [22]
Adipose tissue	$-9.05e^{-6*}$ [21]	$5e^{6}$ [22]	0.01 [22]
Blood	$-0.75e^{-6}$ [26]	5000 [27]	0.7 [27]

Table 2: Electric conductivities, permittivities and magnetic permeabilities of biological tissues as well as for water and saline solution. * -marked values are a general approximation for soft tissues.

Because the magnetic permeability of biological tissue can be rather accurately approximated as vacuum permeability, there is very little information to be found on

the topic. Some literature values are listed in table 2 alongside electric conductivities and permittivities that are more readily found for biological tissues in literature. What is notable for these values, is their dependence on frequency. The values represented in table 2 are taken from values below 100 Hz where these parameters are nearly constant as figure 8 depicts for muscle tissue.

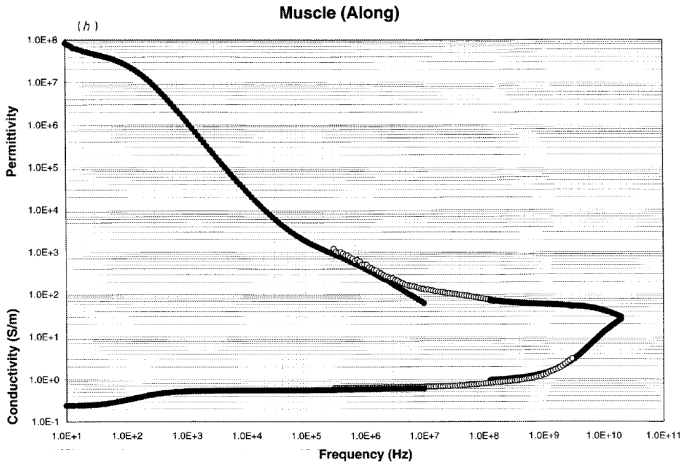

Figure 8: Electric permittivity and conductivity as a function of frequency as measured from bovine muscle along the muscle fibers. [22]

Aside from these material properties, the frequency of the electromagnetic radiation affects how it couples to tissue. As mentioned earlier, the EM spectrum can be divided to quasi-static, resonance and surface absorption ranges all of which have different coupling mechanisms with the human body. At quasi-static range below 30 MHz, electromagnetic fields penetrate unattenuated trough whole body [2, p. 81]. The name quasi-static arises from the fact, that at this range the wavelength of EM radiation is long compared to the measures of a human body, so the radiation can be approximated as static in the length scales of humans. This makes it also possible to treat electric and magnetic waves as separate phenomena [2, p. 39].

At resonance domain, the conductive and capacitive currents elicit strong enough a secondary magnetic field that the induced electric field starts to damp out within the body and the induced current starts to concentrate on the surface [2, p. 98]. This creates damping waves within the body that resonate at suitable frequencies. Together these two phenomena are capable of creating hot spots within the body. On the surface absorption domain the wavelength is also small compared to measures of human body. Because of this, the energy of the radiation is absorbed efficiently to the surface of the body, heating the tissues right at the surface and nearby [2, p. 105]. Since the interest in this thesis is within the ELF magnetic fields, resonance and surface absorption domains are omitted from further discussion.

As the exposure to external EM fields depends not only on the parameters discussed earlier, but also depend on the amplitude and waveform of the external

field, the orientation of the tissue within the field and homogeneity of the field, the quantification of exact dose in a real-life situation is rather difficult. For example, identical exposure can lead to a totally different dose, if the object within the field changes its orientation or if a differently sized and shaped object is exposed. All these parameters need to be taken into account, when considering and comparing the doses.

3.2.2 Biophysical effects of electromagnetic fields

As discussed earlier in chapter 2.1, alternating electromagnetic fields induce electric fields and current densities to tissues placed in them, as suggested by Faraday's law. When sufficiently large, these electric fields and current densities are capable of heating the tissue or distorting cellular activity depending on the frequency of the radiation. The underlying physics and biological basis of these phenomena are well known. Most of the safety limits reviewed in chapter 3.3 are based on either heating effects or distortion of normal neural cell functions.

As described in chapter 2.2, nerve cells can be activated by depolarizing the trigger zone of a neuron above the activation threshold giving rise to an action potential. This activation can also be achieved by an external electric field aligned in axons direction creating an action potential if the activation threshold is reached locally and the voltage-gated gated ion channels opened. The sensitivity of nerve cells for stimulation depends on the duration of the stimulus and currents created by it . The peak value of the induced field plays a more important role in the stimulation ability than the RMS value [2, p. 168].

The electrical excitability of nerve and muscle cell is taken advantage of in various medical treatments and studies. For example in deep brain stimulation electromagnetic stimulation is used to treat Obsessive Compulsive Disorder (OCD) [28]. In spinal cord stimulation, the electromagnetic stimulus is targeted to the spinal cord in order to, for example, treat chronic pain [29]. Another example of the use of electromagnetic fields in stimulating excitable cells is the cardiac pacemaker, which is used to reinstate the proper functioning of the heart [30].

Electromagnetic radiation, depending on the frequency, is capable of heating tissue by the absorption of energy from the electromagnetic radiation or by Joule heating caused by the induced currents. Heating can cause changes to cellular functioning, necrosis, or even result in tissue damage. Cells start to go through necrosis when their temperature rises 5°C, although they can endure temperature rises of tens of degrees if the duration of the thermal transient is sufficiently short [2, p. 150].

ELF EMFs below the stimulation and heating thresholds have also been shown to exhibit biological response. For example Pulsed Electromagnetic Field (PEMF) therapy uses pulsed low amplitude ELF magnetic fields to stimulate cells and tissues. PEMF has been suggested to treat musclosceletal disorders and bone fractures as well

as neurological diseases and chronic pain [31]. Yet the results from various studies concerning PEMF effects are rather contradicting, most likely due to vast variety of parameters used in different experiments. Also low amplitude DC electric fields have been shown to have effects for example on cell migration and wound healing [19]. In both cases, the exact mechanisms of coupling between tissue and electromagnetic fields are yet unknown.

There have been multiple mechanisms proposed to explain the biophysical effects of low amplitude and low frequency magnetic fields from local heating effects to effects of electric forces and more complicated theories like the cyclotron resonance. The physical plausibility of all of these theories have been questioned and none have been experimentally validated. Some examples of proposed theories are collected to table 3 alongside the known problems with the theories.

Hypothesis	Problem
Local heating	Induced fields not large enough
EM forces	Very small compared to biological forces
Cyclotron resonance	Requires too large unconstrained orbits for charged particles
Larmor precession	Requires particle vibration to continue unperturbed longer than plausible
Lednev model	Requires unfeasibly narrow vibrational energy levels and implausible symmetry of the binding of the ions

Table 3: Some examples proposed mechanisms for effects caused by low amplitude magnetic fields and problems with these theories. [2, Ch. 4] [18, Ch. 4]

3.3 Dosimetry in vivo

Dosimetric studies are an important tool in determining safety limits for in vivo exposure to external electromagnetic radiation. In Finland, the radiation and nuclear safety authority (STUK) governs radiation safety. Within EU the standardization is mainly based on safety limits suggested by International Commission on Non-Ionizing Radiation Protection(ICNIRP). Some countries like the USA follow limits suggested by the Institute of Electrical Engineers (IEEE) [2, p. 321].

Since measuring induced currents and electric fields in vivo is rather difficult, [18, p. 85] coupling between electromagnetic fields and human body is studied using computational and physical models. The computational models are mathematical representations of human anatomy used to solve induced fields either numerically or analytically. Physical models on the other hand are physical representatives of human body used in experimental research of dosimetry.

Physical models, also known as phantoms, are used to experimentally study the internal electric fields of a body in an electromagnetic field. Depending on the site

of interest, a phantom can be a model of the whole body or a representation of some part of the body, like the head for example. These phantoms can be solid, semi-solid or liquid representations of the body. Solid or semi-solid phantoms give better approximations of the electrical properties of the body [2, p. 486]. Yet, a liquid phantom is the most practical in some cases, for example when the three dimensional distribution of SAR is of interest.

Early analytic dosimetric models of human body have been overly simplified homogeneous bodies of revolution with constant conductivity [32]. Shapes like spheres, ellipsoids and cylinders have been used to approximate the body or a body part. The induced electric field in an ellipsoid model can be solved as [2, p. 90]

$$E_i(y) = -y\frac{a^2}{a^2+b^2}\frac{dB_0}{dt} \tag{20}$$

where a and b are the measures of the ellipsoid and B_0 the external sinusoidal magnetic flux density. By setting a=b=1, this equation is also applicable for spherical and cylindrical objects. In these cases y is the radius of the sphere or the cylinder. The spherical model is best suitable for modeling the head whereas the ellipsoid model functions best in modeling the trunk as the shapes resemble each other. These different possibilities for the use of equation 20 are presented in figure 9. The cylindrical model can be used to approximate a person standing straight with hands placed along the sides.

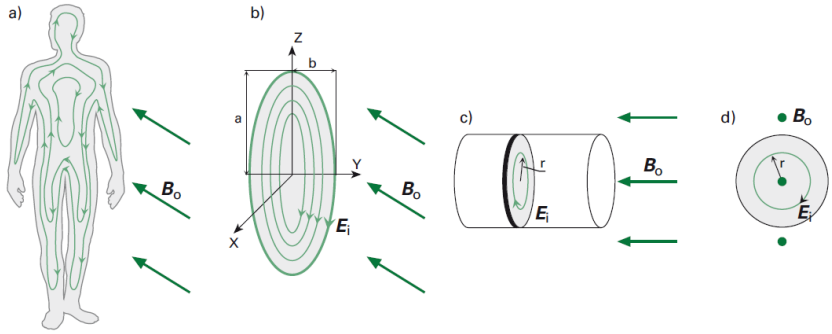

Figure 9: Induced electric field (E_i) in a) body, b) ellipsoid, c) cylinder and d) ball. B_0 denotes the external magnetic field and a and b are the dimensions of the ellipsoid as in equation 20. [2, p. 89]

The actual human body is electrically inhomogeneous and structurally complicated and therefore these simple homogeneous shapes are not suitable models to consider the exact exposure to EM fields. Instead, they can be considered as a simple way for getting information of the average exposure when body is placed within an electromagnetic field [33]. More information from the bodies of revolution can be extracted by using heterogeneous models. For example, SAR in layered lossy ellipsoid has been analytically solved [34]. This model can be used for example to enhance the analytical approximation of arms or legs.

Overall, these simplified geometries are approximative at best even for the given simple geometry [23, p. 35], so accurate anatomical models are vital in understanding the electromagnetic dosimetry better in vivo. Anatomical models are too complicated systems to be solved analytically, so various numerical methods like Finite Difference (FD), Finite Difference Time Domain (FDTD) and Finite Element Method (FEM) have been used to solve the systems [18, p. 78]. The Finite Difference is described as the most prominent numerical method [35] being especially suitable for higher frequency studies [23, p. 38] and also Finite Element Method is also often used [23, p. 39] to solve anatomical models. The Finite Element Method is described in more detail at chapter 4.1 as it is the method used for simulations of this thesis.

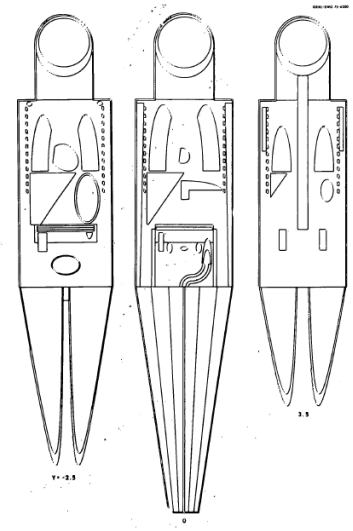

Figure 10: An anatomical model of a 5-year-old as used by Hwang et al. [36] in the seventies. The model is based on simple geometric shapes.

The earliest anatomical models were mathematical models consisting of equations of planes, spheres , cylinders, ellipsoids and so forth to describe internal organs fitted into a torso of elliptical cylinder including embedded volumes to represent bones of arms [35]. The models also included legs, head and neck also build from these simple geometric shapes. Figure 10 illustrates such a model used by Hwang et al. [36] in 1976. These models represent real anatomy only remotely since the shapes are only approximations of the correct shapes of organs, do not fit alongside each other in similar manner than in vivo and the positioning differs also from real life situation [35].

The rise of modern imaging techniques, namely Computer Tomography (CT) and Magnetic Resonance Imaging (MRI) as well as the drastically improved computational power have enabled accurate cross-sectional imaging of human body. These images can be used to create a 3D model of human body, where different tissues are segregated from each other. There are up to 82 different tissues in some models [37] the number being usually around 50 [23, p. 35].

Most anatomical models are voxel-based [37], meaning that the 3D images are segmented with a fixed spatial resolution to create cubical volume elements known as voxels. Compared to mathematical models, voxel models have more realistic shape and organ placement since they are based on images of human body. The shortcomings of voxel models arise from the cubic voxels used, which restrict the resolution of the images used to the size of a voxel. This means that the surfaces are "stepped" which exaggerates the surface area of organs and results in error in thickness of structures thinner than the voxel size like skin or the surfaces of bones [35].

A better level of anatomical precision can be obtained using volumetric or surface description methods [37]. In these methods tissues are converted into closed 3D surfaces instead of voxels to better capture the details of the surfaces. For example, Christ et al. have developed a virtual family of two adults and two children in which the tissues are represented as 3D objects of unstructured triangulated surfaces [37]. One member of the family, Thelonius, is shown in figure 11.

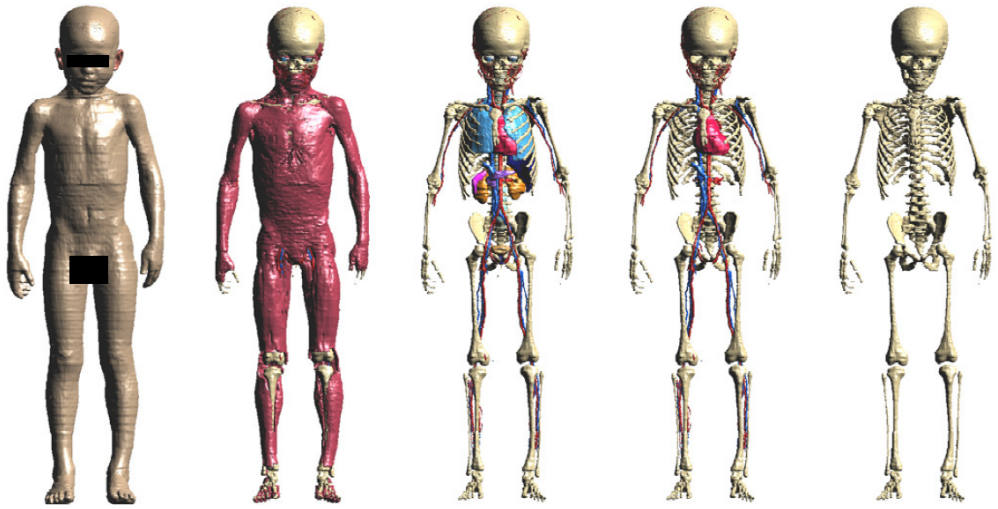

Figure 11: An anatomical model of a 6-year-old boy, Thelonius, from the virtual family project. [37]

Since humans differ in size and shape, too direct conclusion should not be made based on a single human body model. The statistical relevance should be increased by using multiple models. Currently there are only a few dozen anatomical models [37] and more are being developed. Some examples of current models are listed in table 4. Although several automated segregation processes have been developed [23, p. 35], the generation of the models is still demanding and takes lots of time since the segregation of the tissues has to be iterated manually by experienced personnel [35]. This leaves room for human error, since the judgment of the designer is needed to say when the model is correct. Human error can be expected to diminish and accuracy improve as the automated segregation tools become more elaborate. Better segregation tools will eventually enable designing of a population of anatomical models to study dosimetry with improved statistical significance.

Model	Gender	Age	Height	Weight	Project
Duke	Male	34	1.77m	70kg	Virtual Family / Virtual Population v2
Ella	Female	26	1.60m	58kg	Virtual Family / Virtual Population v2
Billie	Female	11	1.46m	36kg	Virtual Family / Virtual Population v2
Thelonius	Male	6	1.17m	20kg	Virtual Family / Virtual Population v2
Glenn	Male	84	1.73m	61.1kg	Virtual Population v3
Fats	Male	37	1.82m	119kg	Virtual Population v3

Table 4: Example anatomical models from ITIS Foundation databases for Virtual population v2 [38] and Virtual population v3 [39].

Based on dosimetric models, ICNIRP has set safety limits for exposure to electromagnetic radiation. Example limits for magnetic and electric fields are presented in figure 12. These safety limits can be divided to basic restriction and reference levels [2, p. 325]. *Basic restrictions* are physical quantities that describe the biological effects in vivo, like the current density and SAR. Since the actual measurement of these is difficult in vivo as earlier is mentioned, *reference levels* for external magnetic and electric fields have been assigned to make it easier to define whether the electromagnetic field is safe. These safety values are meant to protect the population from direct effects on tissue [2, p.326] like neural or muscular activation as described in chapter 2.2.3. The possible effects of low doses or the effects on active implants are not considered. The limits are also set higher for occupational exposure than for the whole population, since the risks for occupational exposure are expected to be better understood as well as the occupational expose is expected to fall only upon healthy adults. Also the time of exposure is expected to be only 8h instead of 24h [2, p. 328] for occupational exposure.

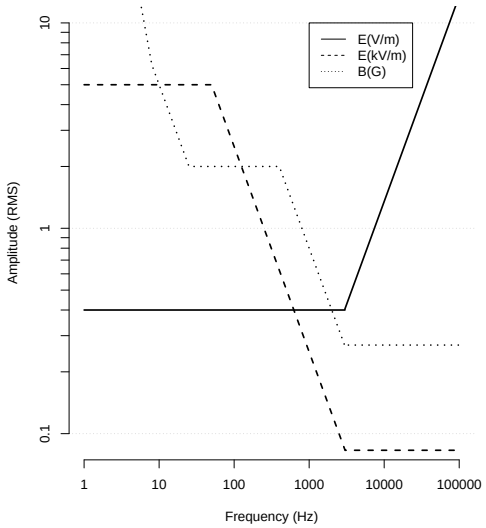

Figure 12: Reference levels (dotted lines) for electric and magnetic fields and basic restriction (solid line) in terms of induced electric field for frequencies below 100 kHz for general population. [40]

3.4 Dosimetry in vitro

In many cases, effects of electromagnetic radiation on biological tissue is difficult to assess in vivo and therefore in vitro models are used to enable more controlled environment for experiments. Also the current legislation is driving experimental research more towards in vitro experiments instead of using animal models [41].

Yet, there are more than a few shortcomings in using in vitro models to describe actual in vivo events. Aside from the homogeneity of in vitro cellular cultures, cells tend to be in a two dimensional layer at the bottom of a cell culture dish instead of natural 3D organization in the body. This also results in cells being of different shapes than they would be in vivo. As already discussed earlier, the shape, size and orientation in external fields affect the induced fields meaning that the induced electric fields and current densities within and among cells can differ between in vitro and in vivo.

Also the environment of the cells of interest differs in vitro and in vivo. The values of typical culture media have been reported to lie around 1.5 S/m [42], which lies in the same region as the conductivities of intra- and extracellular fluids discussed earlier. But where in vivo the surroundings of a single cell are highly heterogeneous, in vitro there is only the homogeneous culture medium keeping the cells viable. This also has an impact on the total distribution of current density as the currents tend to pack into regions of higher conductivity.

By analytical studies and numerical simulations of the different parameters affecting the induced fields, these problems can be addressed and the experiments designed in such a way that the exposure to external electromagnetic fields becomes similar to in vivo exposure. This enables more biologically relevant results and facilitates comparing results from between experiments.

3.4.1 Experimental work

The effects of both electric and magnetic fields have been widely studied on different cell types in vitro.Among these studies a plethora of different parameters have been used without sufficient consideration of the effects of the parameters themselves but rather with the focus of reporting the end effects of stimulation. The uncoordinated use of parameters has resulted in contradicting results, making it difficult to unravel the underlying mechanism of the interaction between ELF EMF and biological tissue.

As already discussed earlier in chapter 2.2.3, endogenous electric fields have been measured in vivo. There has also been interest in DC electric field studies in vitro in order to find how they affect cells. For example, mouse 3T3 fibroblasts have been shown to exhibit directional migration towards cathode under DC electric field of 5 V/m and generally many cell types migrate towards cathode at DC electric fields of 0.1 to 10 V/m [19]. Electric fields have also been suggested, for example, to help embryonic stem cells differentiate into neuronal cells [43].

With magnetic fields, the interest in in vitro studies has been mostly among ELF magnetic fields as they have been shown to treat bone fractures although the mechanisms are not known [31]. The ELF magnetic treatment is often called pulsed electromagnetic field (PEMF) therapy. Whereas the DC electric fields affected the migration of the cells, PEMF has been shown to affect for example in NO-signaling pathways in osteoblasts affecting their differentiation and maturation [44], human mesenchymal stem cell osteogenesis [45] and proliferation and mineralization of osteoblasts [46].

The problem with the stimulation parameters is especially prominent in PEMF studies, where various amplitudes, signal waveforms, orientations of external magnetic field have been used to stimulate different cell types with differing seeding densities and maturation stages on multiple kinds of cell culture dishes for different durations. Also the amount and conductivity of the cell culture medium has varied between experiments. It is therefore obvious, that the comparison of these studies is difficult. The parameters used in ELF EMF are discussed in more detail later in chapter 4.4.

3.4.2 Modeling

The main mode of interaction between magnetic fields and biological tissue is via Faraday induction of electric field resulting in eddy currents as already discussed earlier. Based on this, the parametric problems in ELF EMF studies in vitro can be readily assessed by analytic and numeric modeling of the fields induced on simple geometric shapes of the cell culture dishes.

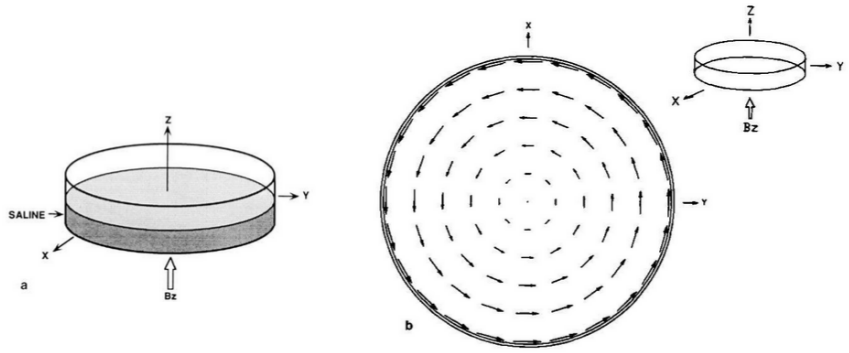

Figure 13: a) A Petri dish filled partially with physiological saline solution and b) the induced electric field distribution on it. [42]

Bassen et al. [42] have studied the induced electric fields in a Petri dish, a Petri dish with annular ring and a tissue culture flask. In the simplest form for a homogeneous circular disk perpendicular to the magnetic field as depicted in figure 13, the induced electric field can be written as [42]

$$E(r) = \pi f r B_0 \tag{21}$$

where r is the radius of the disk. As can be seen from this equation, the relationship between E and B is linear and depends on the radius of the plate and the frequency of the magnetic field it is placed into. The radial dependence makes the distribution of the electric field highly non-uniform on the dish.

The non-uniformity can be addressed by compartmentalizing the Petri dish with annular rings as shown in figure 14. With a single annular ring, the induced electric field within the Petri dish can be written as

$$E_{avg} = \frac{2\pi}{3} f B_0 \left(\frac{r_0^2 + r_o r_i + r_i^2}{r_0 + r_i}\right) \tag{22}$$

where r_i is the inner and r_0 the outer radius. Experimentally Bassen et al. [42] measured ±12% uniformity of the average field in the outer well using this setup.

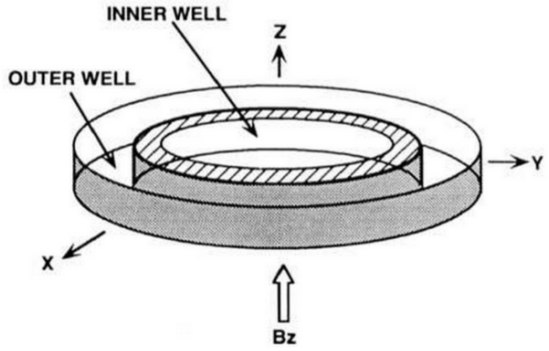

Figure 14: A Petri dish with a single annular ring. [42]

In their paper, Bassen et al. [42] also noted that the sensitivity of induced fields in the Petri dish to the volume of liquid on the dish depends on the orientation of the dish within the external magnetic field. In a perpendicular orientation, meaning that the external magnetic field is directed along the normal of the dish's surface, the induced fields are not sensitive to the changes of volume on the dish. If the dish is in parallel orientation, meaning that the the magnetic field is directed along the radial direction of the dish, the induced fields exhibit a dependence on the liquid volume.

Also the induced electric fields within partially filled tissue culture flasks parallel to the external magnetic fields have been solved analytically [42] to be

$$E_{ymax}(h_{half}) = 2h_{half}\pi f B_0 \tag{23}$$

where the $h_{half}$is the half height of the liquid medium. This equation yields only 0.1% error to the exact analytical solution if h/a is less than 0.3. When h/a is less than 0.1, the electric field is within 8% of the maximal value on 85% of the surface of the flask [42].

The conductivity values of typical culture media have been reported to lie around 1.5 S/m [42].

4 Methods

In order to shed light on the parametric problems of in vitro ELF EMF experiments and the differences between induced fields in vitro and in vivo, a series of parametric Finite Element simulations were carried out. These simulations were conducted for two modeled common in vitro cell culture dishes containing average cell culture medium as well as for a simplistic model of human leg for comparison. As a simulation tool, Comsol Multiphysics 5.0 was chosen due high performance in electromagnetic simulations and simplicity of use for example compared to Abaqus.

4.1 Finite Element Method

As mentioned already in chapter 3.3, there are multiple numerical methods that have been used to study dosimetry. As Comsol Multiphysics simulation software used in this thesis exploits FEM to solve the systems being studied, this chapter presents the method briefly.

Finite Element Method (FEM) is a popular numerical method in physics and engineering for solving boundary value problems governed by partial differential equations and boundary conditions. The main concept in FEM is to divide a geometrical entity into subdomains called elements and to express the governing differential equation along the boundary conditions as a set of linear equations that can be solved by the means of linear algebra [47, p. ix]. The general steps for FE solution are [47, p. 4-5]:

1. Discretize the geometry
2. Choose shape functions
3. Built linear equations for individual elements
4. Assemble the equations to create a global matrix system of equations
5. Solve the system

In the first step, the geometry is discretized into finite amount of elements called the mesh, hence the name finite element method. Each element consists of nodes, which are conformal in traditional FEM. For example with a triangular 2D element this conformality means that each element shares one edge and two vertices with each neighboring element [23, p. 40]. Depending on the geometry studied, the elements can be 1, 2 or 3 dimensional; linear, quadratic or higher order and so forth. Model can consist of different element types and the elements can be of various shapes although the element type is the same allowing the mesh density to be varied around the model. In order to ease the calculations of differently shaped elements, they can be mapped to a master element by coordinate transformation to natural coordinates,.

For example 1D line element shown in figure 15 can be mapped to a master element with transformation [47, p. 6]

$$\xi = \frac{2(x - x_1^e)}{x_2^e - x_1^e} - 1 \tag{24}$$

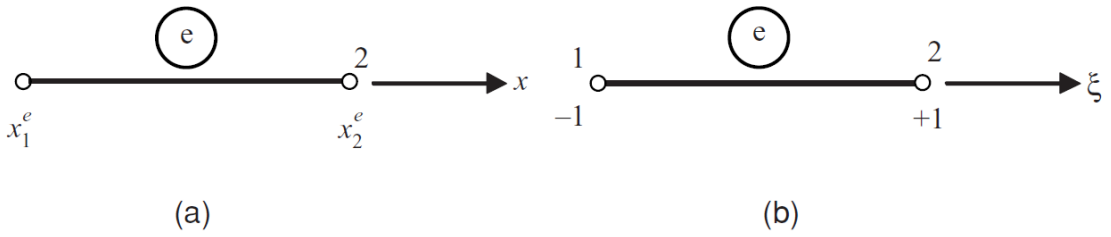

Figure 15: a) 1D element along x-axis. b) 1D master element along ξ-axis. [47, p. 6]

where, ξ is the nodes natural coordinate and x the original coordinate. Subscripts 1 and 2 denote the number of the node and superscript e denotes the element in question.

The unknown quantities are solved at the nodes of the elements and interpolated within the element based on the nodal values solved. For the interpolation, a set of shape functions is needed as step 2 suggests. Shape functions need to be continuous, differentiable and a complete set of polynomials, meaning that they must consist of all the lower order terms [47, p. 6]. For an element, as many shape functions are needed as the element has degrees of freedom, nodes. The sum of shape functions must be equal to one at each point within element, in 3D natural coordinates this can be expressed as

$$^{e}\Sigma_{i}^{n}\ {}^{e}N_i(\xi,\eta,\zeta) = 1 \quad \forall \xi,\eta,\zeta\ \in e \tag{25}$$

where ξ, η, ζ are the natural coordinates, n is the amount of nodes and e is the element in question. For example, the shape functions for the line master element in figure 15 are $N_1 = \frac{(1-\xi)}{2}$ and $N_2 = \frac{(1+\xi)}{2}$.

By using the shape functions the value of the primary unknown quantity X can be stated anywhere within the element based only on the nodal values X_i. Generally this can be expressed as

$$^{e}X(\xi,\eta,\zeta) = \Sigma_{i}^{n}\ {}^{e}X_i N_i(\xi,\eta,\zeta) \tag{26}$$

The finite element equations can be obtained from the original partial differential equation by using either variational method or weighted residual method [47, p. 3]. The variational method requires construction of functional representing the energy of the boundary value problem being solved. The functional is then maximized or minimized with a process involving partial derivatives that can be used to discretize the equations with proper choice of elements and shape functions. The variational method is more complicated than the weighted residual method, but there are cases where it is necessary [47, p. 4].

In the weighted residual method, a weighted residual is formed from the original partial differential equation by transferring all terms on the same side, multiplying them by a weighting function and integrating over the elements domain. If the shape functions are used as weighting functions, the weighted residual method is often

referred as the Galerkin method [47, p. 4]. If the differential equation to be solved is of second order, the shape functions are required to be twice differentiable. This condition can be weakened by partial integration of the weighted residual which results in distribution of the second derivative equally between weight and shape functions [47, p. 4]. This is referred as the weak formulation of the problem as it allows the use of only once differentiable shape functions.

The discretized partial differential function for a single element is of form [47, p. 19]

$$ {}^{e}\underline{\mathbf{K}}^{e}\mathbf{x} = {}^{e}\mathbf{f} \tag{27} $$

where matrix $\underline{\mathbf{K}}$ is often referred as the element matrix, containing the nodal information of the element e, $\mathbf{x}$ is vector of the unknown quantities and $\mathbf{f}$ is a vector of force and flux terms acting on the nodes of an element e. By summing all individual elements together, the global finite element equation of form 28 is obtained and can be solved by the means of linear algebra. Usually the solution is obtained by computers as the systems can have millions of degrees of freedoms in large models.

$$ \underline{\mathbf{K}}\mathbf{x} = \mathbf{f} \tag{28} $$

4.2 Models

Three Comsol models were created for this thesis, two of them being for common cell culture dishes and the third being a section of a leg.

The cell culture dishes chosen for the simulations were a common 10 cm Petri dish and a 48-well dish. From the multiple available radii for Petri dishes, a 10 cm dish was chosen to get a clear difference for the radii of the Petri dish and a single well of the 48-well dish. There are also multiple different multi-well dishes available, the 48-well dish was chosen as a compromise between the amount of wells and the ease of building the model.

Parameter	Value
ϵ_r	2.4 [48]
σ	10^{-18} S/m [48]
χ_M	$-0.75e^{-5}$ [49]

Table 5: Electric and magnetic parameters for polystyrene.

For both cell culture dishes, only the liquid portion was modeled as the plastic container itself was assumed to have no effect on the results due to low conductivity, electric permittivity and magnetic susceptibility of common plastics. As an example, these parameters for polystyrene used by Thermo Fischer Scientific [50] in their Petri dishes are listed in table 5.

The meniscus of the liquid was not considered in the model to simplify the meshing of the model and it was also assumed to have negligible effect on the currents at

the bottom of the disc where the cells are located. The cell-layer at the bottom of the culture dishes was omitted as well, although the current densities experienced by the cells is of interest for this thesis. This was done to simplify the model as implementing small cells at the bottom of the dish, even if they were of a simplified shape and composition, would explode the size of the models due to large differences in length scales of the objects within the model. It is possible that this results in underestimation of the current densities at the cellular level as the poorly conductive cell membranes pack the electric currents to the small gaps of well conducting cell culture medium in between them. The cell culture dish models alongside the parameters for the models are shown in figures 16 and 17 and tables 6 and 7.

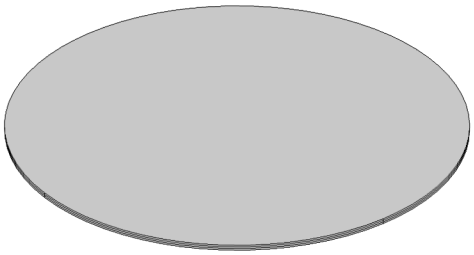

Figure 16: The model of a Petri dish used for the simulations.

	Measure
Diameter	100 mm
Height	1.2 mm
Volume	10 ml

Table 6: The measures of the Petri dish model

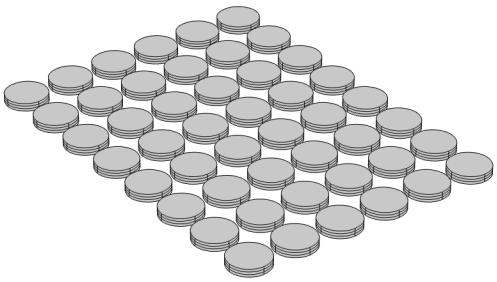

Figure 17: The model of a 48-well dish used for the simulations.

		Measure
Well	Diameter	11 mm
	Height	2.1 mm
	Distance	2 mm
	Volume	2 ml
Dish	Width	76 mm
	Length	102 mm

Table 7: The measures of the 48-well dish model. Distance means the distance between two wells.

A simplified cylindrical model of a leg was also created in order to get approximations of actual in vivo induced fields for comparison. The model used is a 5cm thick section of an adult leg, created by using the diameter of author's right leg as a scale and proportions from figure 18a to get dimensions for the thicknesses of skin and adipose tissue as well as radii for tibia, fibula and the two large veins. The model built is shown in figure 18b and the dimensions in table 8.

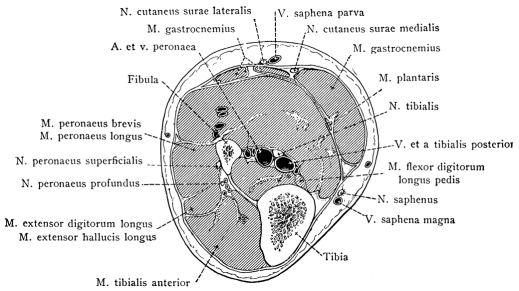

(a) A cross-section of a leg.

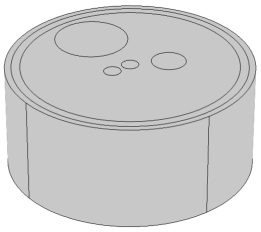

(b) The model-leg.

Figure 18: A cross section of a leg [51] and a simplified Comsol model built based to it.

	Diameter	Height
Leg	114 mm	50 mm

	Thickness
Skin	3 mm
Adipose tissue	4 mm

	Diameter	Location
Tibia	32 mm	(0,0.03) m
Fibula	16 mm	(0.016,-0.008) m
Vein 1	8 mm	(0,0) m
Vein 2	8 mm	(-0.01,0) m

Table 8: Parameters used in the leg model.

4.2.1 Meshing

Dish	Layers	Element size	Domain elements
	1/2		11752/40598
Petri dish	3/4	normal	60204/82504
	1/2		6336/28186
48-well dish	3/4	fine	88178/ 141444
		extra coarse / coarse	4821/14466
Leg	1	fine / extra fine	40486/194394

Table 9: Mesh parameters for tested meshes

To obtain a sufficient mesh density a series of test simulations with different mesh densities were run using 50 Hz and 10 G sinusoidal magnetic field perpendicular to the dish as an input. For the cell culture dishes, the mesh density was modified by using 1 to 4 layers in the models of cell culture dishes while keeping the Comsol's mesh density setting constant. Different amounts of layers were used as Comsol would use only one layer of elements otherwise due to the plates being thin compared

to the diameter. Four different densities of mesh were used for the leg model using only one manual layer in the leg model as the model was thick enough for Comsol to adjust the amount of elements in all three dimensions. For all simulations, free tetrahedral meshing was used. Table 9 presents the mesh parameters tested.

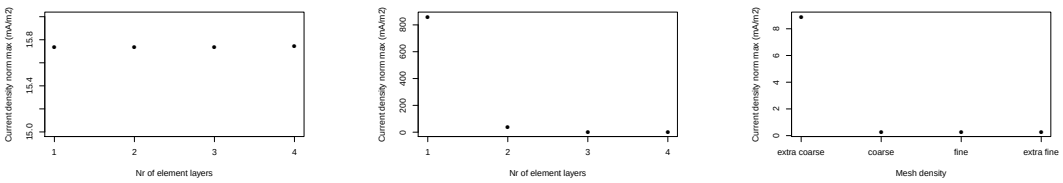

(a) Petri dish (b) 48-well (c) Leg

Figure 19: Induced current density as a function of mesh density on different models.

As can be seen from figure 19, the induced currents in Petri dish model stay stable when changing the mesh accuracy but with 48-well dish and with the leg model, the less accurate meshes result in very high induced current densities that become lower and more stable as the amount of layers and elements grow. The differences between the two most accurate meshes being 0.03%, 43.6% and 1.3% respectively. The error on the two highest mesh densities of the 48-well dish is large, but the error rises from unstable spatial development of the current density on the mesh densities tested as demonstrated in figure 20.

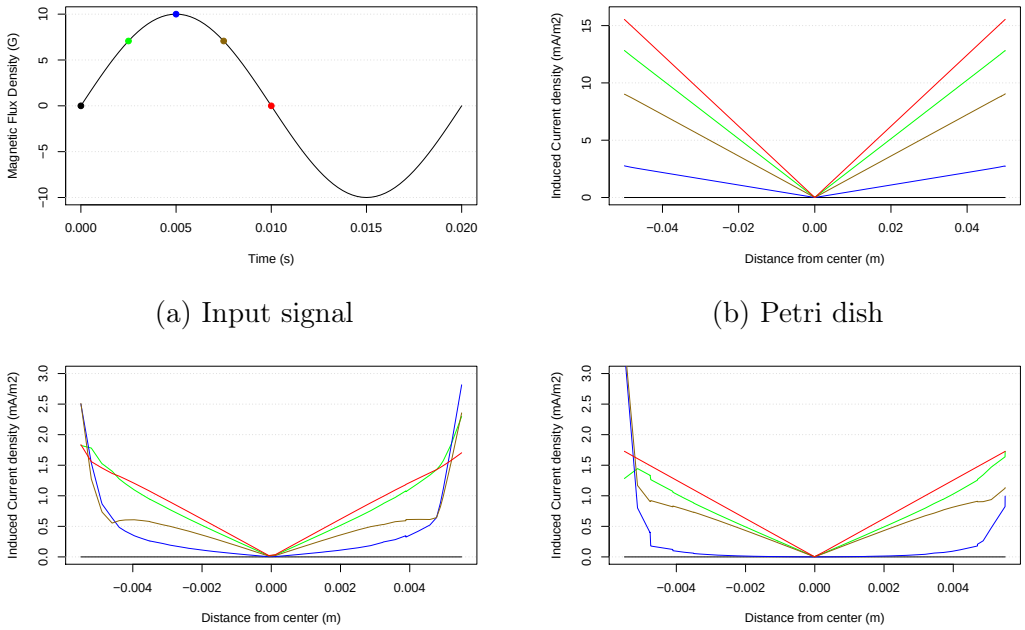

(a) Input signal (b) Petri dish

(c) 48-well dish, 3layers (d) 48-well dish, 4layers

Figure 20: Development of spatial current density distribution on 48-well dish meshed with 3 and 4 layers and on Petri dish.

The instability of the spatial distribution development arises from still too inaccurate a mesh as demonstrated in figure 21 by comparing two simulations of a single well from the 48-well model, one meshed with 3 layers and fine as in previous test and the other as 3 layers and extra fine mesh. Yet, this inaccuracy at the spatial development is not relevant for this thesis as the maximal values are used for comparing the results to each other and to literature values. The highest current density should be induced at the time when the change rate of the external field is the highest according to Faraday's law, meaning that for sinusoidal magnetic field, the time for half wavelength is the most relevant. At this time point, 10 ms for 50 Hz signal, the error between the 3 and 4 -layer simulations is only 0.45% and between the single well simulations 0.2%.

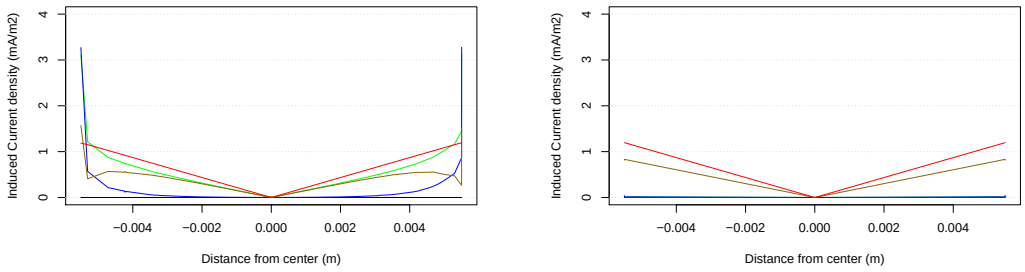

(a) Coarse mesh

(b) Fine mesh

Figure 21: Evolution of spatial distribution of induced current density at two different mesh densities simulated with 1 well model.

Based on these results, the Petri dish and the 48-well dish were decided to be modeled with three layers. Although the Petri dish model showed only a 0.03% of an error in between 1 and 4 layer models, the 3 layers was chosen as a compromise to ensure that any vertical information was not lost. Similarly, the 3 layers chosen for 48-well dish is a compromise, as the mesh density is not enough to capture the temporal development of the spatial current density distribution correctly but still the maximal induced fields have an error of only 0.45% thus giving accurate enough results and at the time keeping the computational effort at reasonable level. For the leg model, fine mesh was chosen as it resulted only in an error of 1.3% to higher mesh density thus optimizing the accuracy to computational efficiency.

4.3 Material parameters

To be able to simulate external fields interacting with systems accurately it is important to know the involved material parameters as accurately as possible. As described already in chapter 3.2.1, the primary properties affecting the tissues coupling with electromagnetic fields are the magnetic permeability μ, electric permittivity ϵ and electric conductivity σ. The effect of changing these variables to the simulation results was studied using the Petri dish -model excited by 50 Hz sinusoidal magnetic field of 10 G perpendicular to the dish and the results are shown in figure 23.

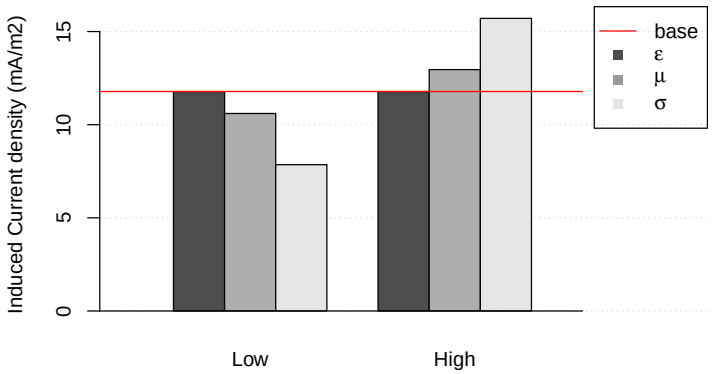

Figure 22: Effect of changing the material parameters onto the simulation results. The baseline result is obtained using $\mu_r = 1$,$\epsilon_r = 75$ and $\sigma = 1.5S/m$, the low values are $\mu_r = 0.9$,$\epsilon_r = 25$ and $\sigma = 1S/m$ and the high values are $\mu_r = 1.1$,$\epsilon_R = 8e7$ and $\sigma = 2S/m$. The low and high value simulations were run by changing each value on its own and keeping the others at the baseline level.

As can be seen from this figure, changing electric permittivity has no effect on the induced current density norm maximum amplitude where as changing electric conductivity and magnetic permeability affects the induced fields. For electric permittivity, the induced current density on all values tested was 11.781 mA/m^2. Changing the conductivity resulted in a linear change in the induced current density with a slope of 7.854 mA/1 and changing the magnetic permeability resulted also in linear change with a slope of 11.781 mA/1. Yet, as discussed already in chapter 3.2.1 the magnetic susceptibilities of water and biological tissues lie in the range of $10^{-5} - 10^{-6}$ giving error of approximately 12-120 pA/m^2 if the magnetic permeability of vacuum is used instead of the correct physiological value. This leaves the electric conductivity as the only parameter having considerable effect on the simulation results in the range of physiological values.

As the electric conductivity is the only significant electric parameter for magnetic simulations, conductivities of five cell culture media was measured. The electric conductivity was measured using *Teopal Consort C533* -conductivity meter with *Teopal SK20B* probe. All media measured were excess from experiments in 50 ml FALCON tubes. The volumes of the liquids varied from 12.5 to 32.5 ml. The measured electric conductivities are listed in table 10. All the values measured are similar to the 1.5 S/m approximated by Bassen et al. [42] discussed at chapter 3.4.2 suggesting that the measured values are reliable.

The average of the measured cell culture media conductivities and the magnetic susceptibility, electric permittivity and thermal properties of a saline solution were used to approximate an average cell culture medium. As discussed earlier, the magnetic susceptibility and the electric permittivity could be approximated as the saline solution parameters as the electric conductivity of the medium was the only

parameter effecting the simulation outcome notably. The exact parameters used for the cell culture medium (CCM) are listed in table 11.

Medium	Conductivity (S/m)
Osteo McCoys (Sample 1)	1.45
Osteo DMEM	1.38
Osteo McCoys (Sample 2)	1.48
DMEM control	1.25
α-MEM	1.42
Average	1.386

Table 10: Measured conductivities of various cell culture media and their average. Alpha Minimum Essential Medium (α-MEM, Gibco, Custom Product, Catalog No. A1049001 from Life Technologies, Gaithersburg, MD) and McCoy's 5A (Life Technologies) were both supplemented with 10% fetal bovine serum (FBS, Gibco), 100 U/ml penicillin, and 0.1 mg/ml streptomycin antibiotics (PenStrep, Life Technologies). The media marked with Osteo were additionally supplemented with 10 mM beta-glycerol phosphate, 0.05 mM ascorbic acid and 100 nM dexamethasone (all from Sigma-Aldrich, St. Louis, MO, USA) solved in 0.2% of ethanol. The control media also contained the 0.2% of ethanol.

For the leg model literature based values were used. All the regions in the leg model were assigned to be composed of a single homogeneous isotropic material apart from the muscle, in which different parallel and perpendicular conductivity of the muscle fibers was taken into account. This is because the orientation of exciting field was one parameter of interest and the conductivity of muscle differs parallel and perpendicular to the muscle cells. All parameters for the tissues, except for blood, were extracted from the extensive databases of Comsol Multiphysics 5.0 and Gabriel et al. [22]. Due to restriction in the Comsol numerical solver, the conductivity of skin had to be raised from $4e^{-4}$ S/m suggested by [22] to 0.001 S/m in order to avoid convergence problems in the simulations. The values used are listed in table 11.

Material	ϵ_R	χ	G [S/m]	$\rho[kg/m^3]$	C [J/kgK]	k [W/mK]
CCM	75 [52]	-1.11e^{-5} [53]	1.386[Measured]	1152 [54]	3410 [54]	0.48 [54]
Bone	800 [22]	-8.86e^{-6} [21]	0.02 [22]	1908 [55]	1313 [55]	0.32 [55]
Muscle	8e^{7} [22]	9.05e^{-6} [21]	$\parallel$ 0.3 [22], $\perp$ 0.1 [22]	1090 [55]	3421 [55]	0.49 [55]
Skin	1e^{5} [22]	-9.05e^{-6} [21]	0.001*	1109 [55]	3391 [55]	0.37 [55]
Adipose tissue	5e^{6} [22]	-9.05e^{-6} [21]	0.01 [22]	911 [55]	2348 [55]	0.21 [55]
Blood	5000 [56]	-0.75e^{-6} [26]	0.7 [56]	1000 [57]	4000 [57]	0.5 [57]

Table 11: Material parameters used for simulations within this thesis. Value marked with * had to be raised so that simulations would converge.

The material parameters for biological tissue are difficult to measure. Often material parameters are obtained by measuring tissue specimens of cadavers or animals [22] as

the measurement procedures of these parameters cannot be conducted in vivo. It is obvious that the parameters measured in cadavers may differ from the values of living tissue in vivo. The parameters of tissues also vary between species. For example, pigs are often used as an animal model for electric parameters of tissues [22, 56] although they do not sweat [58] meaning that the skin conductivity values are likely to differ from humans. The values are also often used in simulations to approximate heterogeneous entities, like the skin, as a single homogeneous unit in order to simplify the simulations. The difficulty of measurement and the computational simplifications result in the material parameters being the best approximations available instead of exact in vivo values.

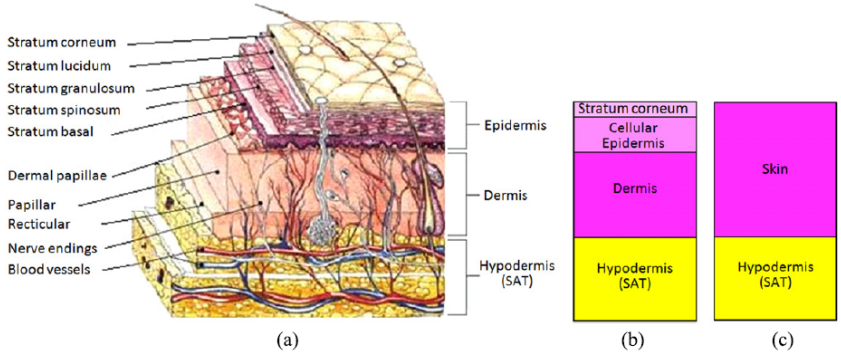

Figure 23: a) The anatomical structure of the skin. b) Simplified three-layer model of the skin and c) simplified single-layer model of the skin

For example, the skin conductivity values measured by Gabriel et al. [22] used also in this thesis have been argued not to give correct results if used in a single layer skin model. A recent study [59], has questioned the usability of these values in ELF EM dosimetry as their study showed that the low conductivity value of stratum corneum would affect the results in regions where electric field is orthogonal to the skin layers. Instead, they suggested the use of the conductivity of dermis, lying around 0.1 to 0.7 S/m, for the skin layer in order to obtain more representative results. Although a variation of the conductivity measured by Gabriel et al. is used within this thesis, the effect on the induced fields is assumed to be negligible as there are no electric fields orthogonal to the skin layer in the simulated section of a leg. Also the simplicity of the model and the permeability of tissue to magnetic fields in ELF range supports the usability of electric conductivity measured by Gabriel et. al.

4.4 Simulations

In total 89 simulations were conducted for this thesis. In the simulations, effects of varying frequency, waveform, orientation and amplitude of magnetic field was studied in terms of induced current densities and electric fields on the three different geometries presented in chapter 4.2. Also the heating generated by sinusoidal 10 G magnetic field was studied. A full list of simulations run can be found from Appendix A.

In literature, low amplitude ELF EMFs have been studied with a plethora of different parameters. Waveforms used in these studies include continuous sinusoidal [60, 61], triangular [46, 62], square [46], serrated [46] and a "Bone growth signal" [63, 64], which is a pulsed pseudo 15 Hz signal consisting of 5 ms bursts of 200 μs pulses with 28 μs intervals. [65] The interval of the bursts is approximately 61 ms. Frequencies used in ELF EMF studies range usually from around 5 Hz [66] up to 100 Hz [66, 67], being most often around 50 to 60 Hz [60, 61, 66, 67]. The EMF amplitudes used in literature range from 1 G [60] to up to 38 G [62], the amplitudes being most often between 5-6 G [67, 68] and 18 G [46, 69]. Also the orientation of the cell culture dish in the external field varies between parallel [46, 67] and perpendicular [60, 64, 69] orientations. As the rise time of external field affects the induced field according to Faraday's law and it has been claimed to be an important parameter for a square waved signal [70, 71], it is also tested via simulations.

	Parameters used in simulations
Waveform	Sinusoidal, Triangular, Square and "Bone growth"
Frequency	10, 50, 75 Hz (mf) & 500, 1000 Hz (ht)
Risetime	0.5, 1, 3, 5 ms
Orientation	$\parallel$ and $\perp$
Amplitude	1 and 10 G
Geometry	Petri dish, 48-well dish, Leg
Simulation types	magnetic fields (mf) and heating (ht)

Table 12: Different parameters used in simulations

Based on the literature values, parameters where chosen for the simulations. From the waveforms, the serrated wave was omitted from this thesis as it can be seen as a combination of triangular and square waves and thus expected not to give new information on the topic in the simulations. Based only on simulations values, the serrated wave should not be omitted from experiments as it is not known whether the induced fields are biologically significant. It is possible that the serrated magnetic field itself affects the cells directly in some manner, even if from a simulation point of view it is unlikely to differ from triangular and square waved magnetic fields. From the frequencies a set of a low (10 Hz), medium (50 Hz) and high (75 Hz) were chosen alongside a low (1 G) and an average (10 G) amplitudes for the magnetic field density. The complete set of parameters used are listed in table 12.

All the magnetic field simulations studying the induced fields were run with the Comsol iterative solver with strict time steps and approximately 80 steps per wavelength, to avoid non-intentional averaging of possible transients in the induced fields. In most simulations the lengths of time steps were left for software to decide but in case of convergence problems, the maximal time steps were restricted below the time scale at which the results were saved. The normal time steps for different waveforms are listed in table 13.

Frequency	Timestep (ms)
10Hz	2.5
50Hz	0.25
75Hz	0.166
"Bone Growth"	0.01

Table 13: Time steps used for simulations on different frequencies

Simulations were run for a single wavelength of the external magnetic field in order to optimize the resolution/memory ratio except for the bone growth signal in which the time steps necessary were so small that simulating a whole wave length would have resulted in impractically large result files. The induced current densities were exported from Comsol and post processed with R (3.0.2). The maximum induced current density on the plate is used as the main parameter in comparison between different simulations as well as the spatial and temporal distributions of the induced fields extracted from the data.

The thermal simulations were run using the Comsol frequency transient simulation with the Petri dish model. The simulation was carried out with 10 minute time steps for 8 hours, the initial temperature of the liquid being 310.15 K and the external sinusoidal magnetic field density of 10 G perpendicular to the dish. The conduction and radiation of heat away from the liquid was not taken into consideration, so the simulation results are very conservative. Thermal simulations were run with higher (> 500 Hz) frequencies than the ELF range due to some convergence issues at lower frequencies.

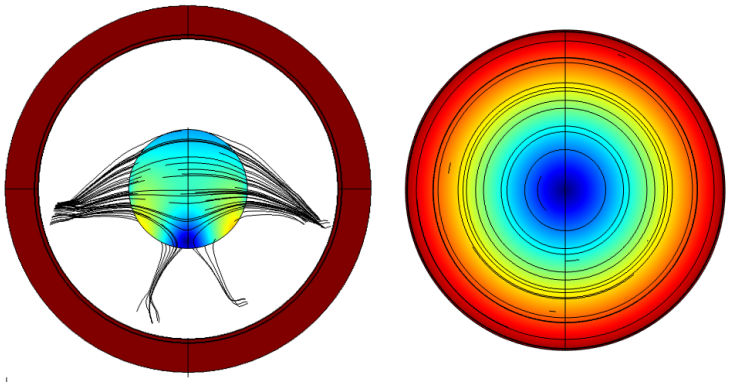

(a) Failed (b) As predicted

Figure 24: Plots of the a) failed and b) working simulations setups. The black lines on the figures show the trace of the currents flowing in the Petri dish.

Due to restrictions of the Comsol numerical solver, the external magnetic the field was applied as a boundary condition instead of simulating a full coil system. As the Comsol numerical solver requires that the ratio of highest and lowest conductivity in the model is not too large, the use of almost a perfect an insulator like the air will cause numerical error in the simulation, unless some artificial conductivity is

assigned to it [72]. The use of an artificial conductivity for air in a model containing Helmholtz coil with copper wiring and a Petri dish in an air-filled incubator leads to leakage currents in the air, strongly disturbing the distribution of currents on the plate as shown in figure 24.

As cell culturing is conducted within steel-walled incubators which could not be included into model due to afore mentioned issues with air conductivity, the effect of incubator walls on the magnetic field created by Helmholtz coil was assessed in order to find out whether it needs to be taken into consideration in the simplified models. The simulated errors in magnetic flux density created by a current of 1.373 A running within Helmholholtz coils (radius of 14 cm, 125 rounds) within an incubator and in free air, are plotted in Figure 25 alongside a figure of the model itself. As can be seen, the effect of incubator for the magnetic flux density is negligible, resulting in 0.7% error for all waveforms tested at the center point of the Helmholtz coil.

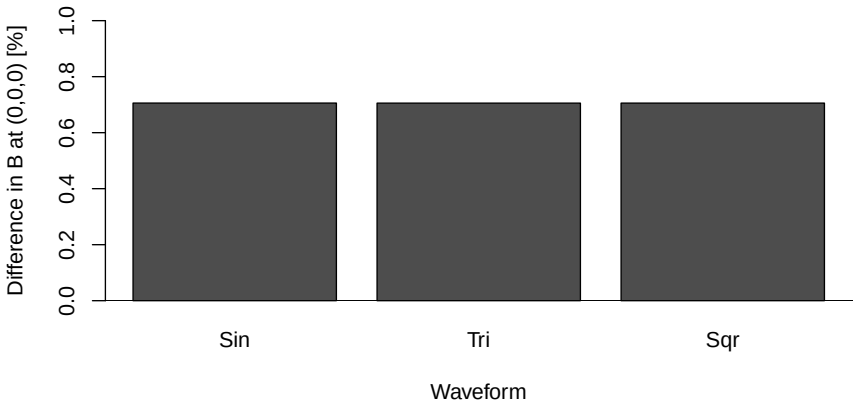

Figure 25: The error of the magnetic field density at the center point of a Helmholtz coil system between simulations with and without surrounding steel walls

4.4.1 Data

For post processing, data of chosen spatial and temporal points was exported from Comsol Multiphysics. Figure 26 shows the lines and points from which the data was used for post processing. Spatial distribution of induced current densities at all timesteps was obtained from the lines and the temporal behavior of the induced current densities was extracted from the points. Induced current density was chosen as a parameter of interest as it is one of the main parameters used to describe ELF EMF dosimetry and endogenous current densities were available for comparison. Based on the literature values endogenous currents, the simulation results can also be used to argue whether the induced fields can theoretically elicit biological response.

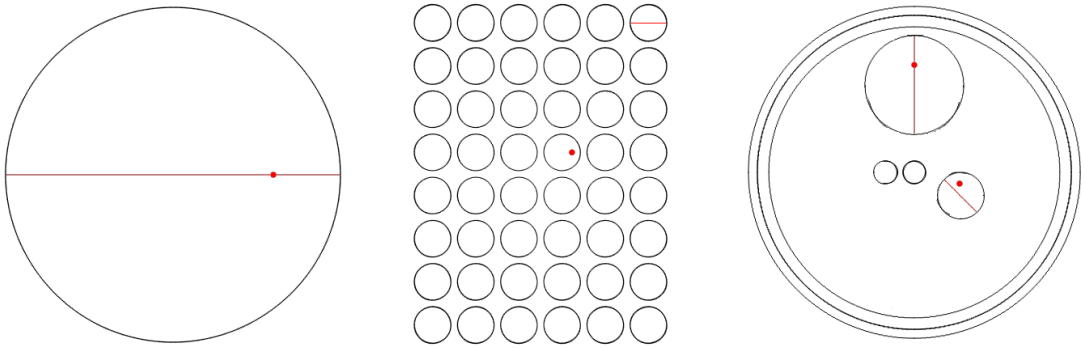

(a) Petri dish (b) 48-well (c) Leg

Figure 26: Lines and points for data extraction from the models.

For Petri dish, spatial data was obtained from the x-axis crossing the model and the temporal data was extracted from point (0.03,0,1e-6) m. For the 48-well dish, a single well was chosen to extract the spatial data from a line running through its diameter and another well from which the temporal data was extracted at point (0.0095,0.0065,1e-6) m. The 1 μm above the bottom is approximated from the length scales of cells to be amongst the cell layer at the bottom of the dish. For the leg model, data was extracted from the two bones of a leg, Tibia and Fibula, as ELF EMF is often used to treat bone fractures in vivo. This model gives therefore a reasonable point of comparison for the cell culture dish simulations. Again, the lines and points ((0,0.038,0) m for tibia and (0.016,-0.004,0) m for fibula) from which the data was extracted are shown in figure 26. The lines chosen were radial to the leg cylinder.

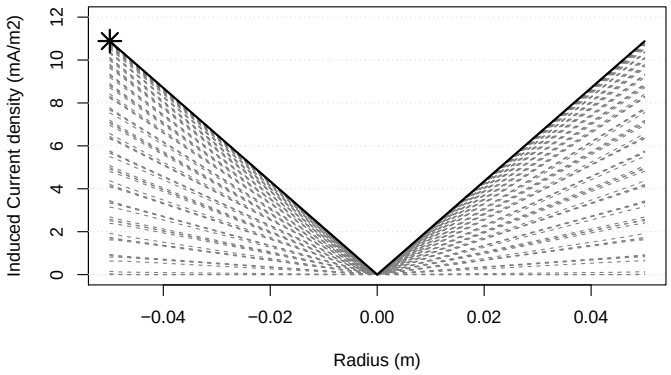

Figure 27: The spatial distribution of currents on the Petri dish model at all time points. The solid black line shows the distribution at time point of half wavelength and the star shows the maximum found by the R script.

The maximum amplitudes for Petri dish, Tibia and Fibula were obtained from data of the current density on the lines shown in figure 26 at all time steps. The maximum was then searched from these data with R (3.0.2). An example of the process is

shown in figure 27. The maximums for 48-well dish were obtained from the line data at half wavelength-time step for reasons explained earlier.

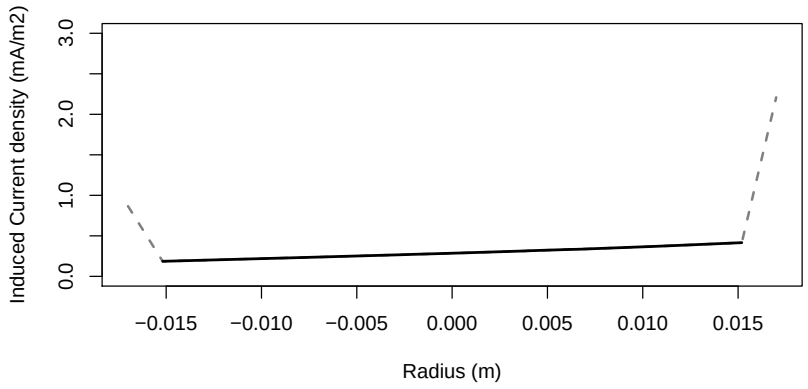

Figure 28: The transients occurring at the edges of bone and muscle tissue in the leg model (grey dotted line) and the part of the spatial distribution used for analysis (solid black line).

The bone data obtained contained transients at the boundary between the muscle and the bone as shown in figure 28. These transients were omitted from the analysis of the data as they are strongly affected by the muscle surrounding the bone and therefore do not reliably represent the currents at the bone.

4.5 Error sources

Although simulations are a powerful tool in understanding physical phenomena, there are a multitude of error sources and simplifications involved in the work. Error inherently arises from the actual computer modeling process of the geometry of interest. Some of this error results from measurement of the object modeled but unless the geometry is simple, simplifications are often made to it in order to reduce computational costs and time to create the model. Especially very large differences in the length scales of the model, like different layers in skin or membranes over organs compared to the organ itself, are often omitted from simulations as they would be too much of a burden computationally. The simplifications in the modeling of this thesis has already been discussed in chapter 4.2.

In FEM, the discretization of continuous media into finite elements gives rise to discretization error depicted in figure 29. To address this problem, the size and order of the elements can be adjusted to decrease the error but care should be taken in order to avoid raising the computational costs of the model higher than necessary. Some error sources are also connected directly to the numerical methods used for solving the problems.

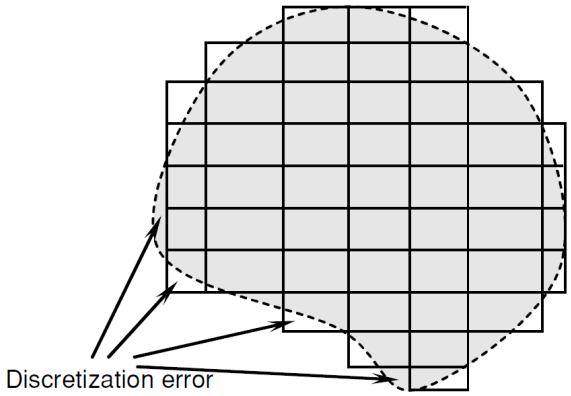

Figure 29: Discretization error when discretizing an irregular 2D object with rectangular elements. [47, p. 53]

Another significant error source for simulations comes from the material parameters and models used to describe the materials involved in the simulation. Material properties are often not constants but vary for example over time, temperature or frequency. Also, the material properties are not always isotropic, meaning that the property is varies by orientations as in the case with electric conductivity of the muscle. These dependencies make the measurement of the exact material properties of some materials complicated and therefore difficult to find in literature. In biological tissues error also rises from the measurement of the material properties, as it often has to be done using tissue samples from cadavers or animals as the measurement is not possible in vivo. Overall, the used material properties in simulations are often best approximations available and often approximated as isotropic constants either as a simplification for the model or due to scarcity of the information available. The simplifications regarding material parameters used for this thesis have been addressed in chapter 4.3.

5 Results

5.1 Temporal behavior and maximal amplitudes

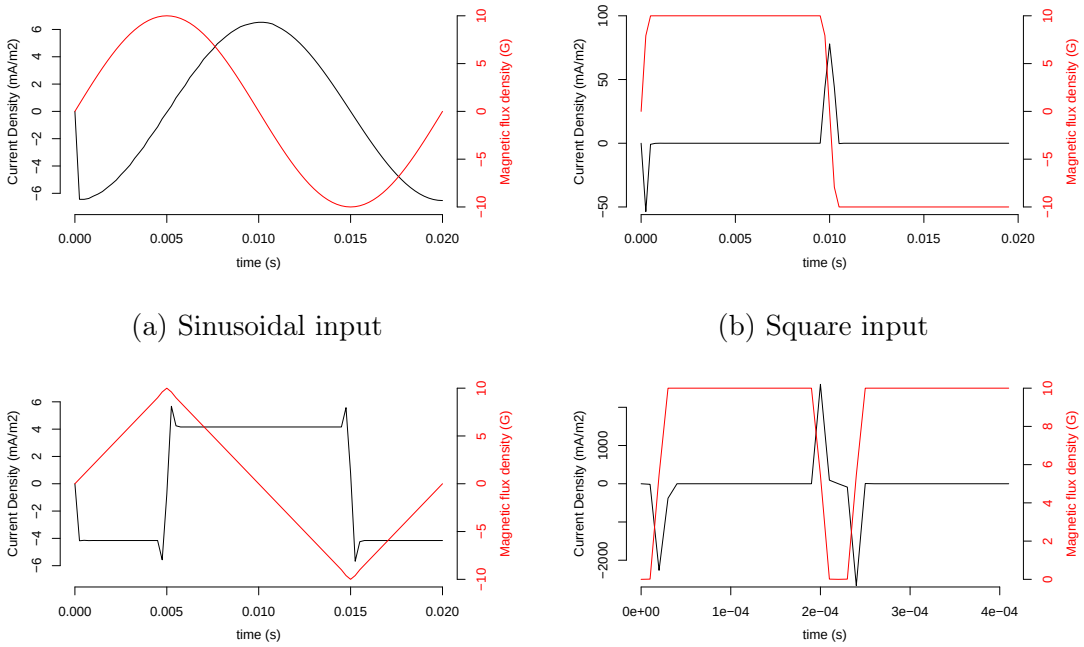

(a) Sinusoidal input

(b) Square input

(c) Triangular input

(d) Bone growth signal -input

Figure 30: Magnetic field inputs (red lines) and corresponding induced current densities (black lines) for the magnetic field waveforms used in this thesis.

The temporal behavior of the signals used within this thesis are plotted in figure 30. As can be seen from these figures, the temporal behavior of the induced current densities vary strongly as different input shapes are used. This behavior is expected as Faraday's law states that the induced fields are dependent on the rate of change of the external field. Sinusoidal input results in sinusoidal output with a slight change in phase, triangular input gives a square-like output with transients near the peaks of the input signal. These transients are omitted from further analysis, as they result from numerical error at the abrupt discontinuity near the peaks. The data in following results and discussion is obtained from half-wavelength -time point giving stable results as figure 30c shows. The square wave and bone growth signal give similar outputs: sharp spikes at the sites of changing field. This is expected, as both waveforms are squares differing only in rise, up and down -times.

Areas under the curve were calculated for the induced current densities in figure 30 with R (3.0.2) package MESS to quantify the temporal behavior of the induced fields. As can be seen from the results listed in table 14, the waves form two pairs, sinusoidal and triangular give similar AUCs and also square wave and bone growth signal give similar AUCs, the latter being slightly smaller.

	AUC
Sin	82.32390
Tri	82.45901
Sqr	55.09934
Bone	53.53110

Table 14: Areas under the curve for induced current densities at figure 30.

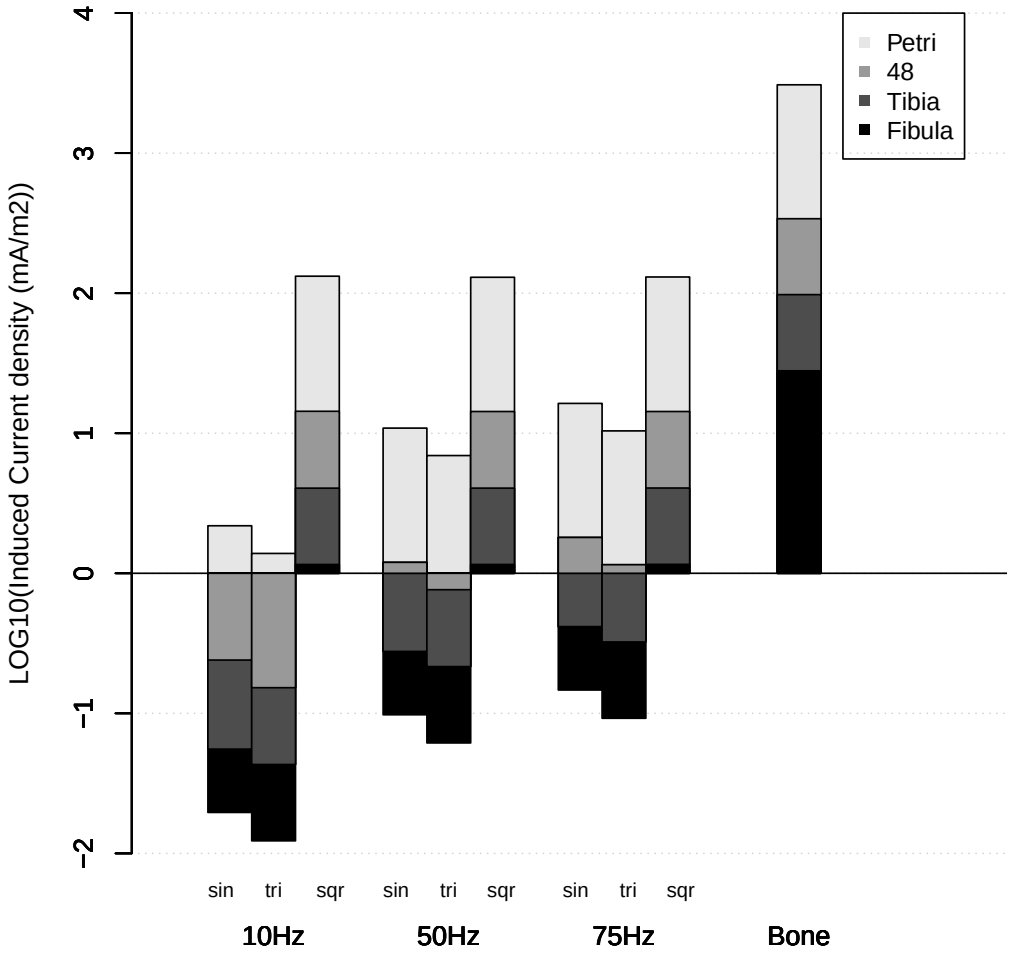

Figure 31: 10-based logarithms of maximal amplitudes on dish for all the waveforms and frequencies used.

10-based logarithms of induced current density maximums on different waveforms, frequencies and platforms are presented in figure 31. As can be seen from this figure, the highest amplitudes on all dishes were obtained using a bone growth signal, a special case of square wave.

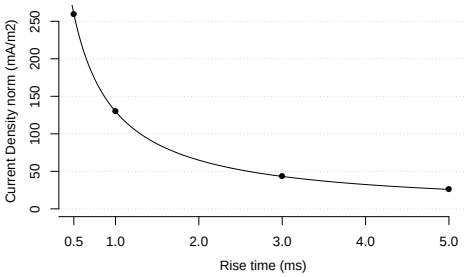

Figure 32: Effect of risetime of square wave to the induced current density.

Aside from the bone growth signal, the square waves in general give the highest amplitudes on all studied platforms. The resulting maximum amplitudes of the square waves are independent of the frequency, differing only 1.8% between the highest and lowest value induced on different frequencies. The difference between square wave signals and the bone growth signals is the rise time of the signal(1 ms and 0.01 ms, respectively), which causes the bone growth signal to give higher amplitudes as it has a more rapid rise time compared to the square waves used. The effect of rise time on the maximal amplitude of induced current density is clarified in figure 32.

The effects of radius of the plate as well as the effect of frequency on the induced fields are also apparent from figure 31. For all frequencies and waveforms, the highest induced fields are obtained with Petri dish having largest radius followed by the 48-well dish and the two bones in the order of their size. The reason for 48-well dish having higher induced fields than the bones although it has smaller radius is the higher conductivity of the cell culture medium compared to the bone.

The induced field amplitudes also grow linearly as function of amplitude as is clarified in figure 33 comparing the normalized electric current densities induced from 1 G and 10 G magnetic fields. The normalization for each case is obtained by dividing both the 1 G and 10 G induced field by 1G induced field and thus obtaining how many times larger field is induced by using 10 G field than is induced by using 1 G magnetic field. As can be seen from the figure, the relationship between induced fields and the external magnetic field is linear with all waveforms and all models meaning that increasing magnetic field tenfold results in ten times larger induced fields.

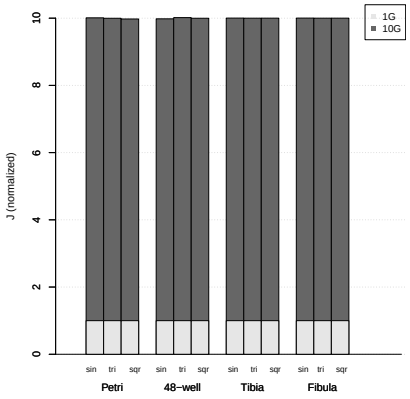

Figure 33: Amplitudes of induced current densities on different vessels and magnetic field waveforms with two different magnetic field amplitudes normalized to the current density induced by the 1 G magnetic field.

Numerical values of the maximal induced current densities on different vessels, frequencies and amplitudes are listed in table 15.

			Petri dish	48-well dish	Tibia	Fibula
	10 Hz	10 G	2.184	0.420	0.056	0.020
	50 Hz	1 G	1.087	0.120	0.028	0.010
Sin	50 Hz	10 G	10.885	1.197	0.277	0.098
	75 Hz	10 G	16.331	1.803	0.416	0.147
	10 Hz	10 G	1.385	0.152	0.043	0.012
	50 Hz	1 G	0.693	0.076	0.022	0.006
Tri	50 Hz	10 G	6.929	0.763	0.216	0.061
	75 Hz	10 G	10.395	1.151	0.323	0.092
	10 Hz	10 G	132.280	14.350	4.054	1.156
	50 Hz	1 G	13.025	1.430	0.406	0.116
Sqr	50 Hz	10 G	129.939	14.293	4.056	1.156
	75 Hz	10 G	130.575	14.295	4.064	1.158
Bone	-	10 G	3076.563	340.349	97.675	27.923

Table 15: Induced current density maximums [mA/m^2] at Petri dish, 48-well dish and on tibia and fibula with different signal waveforms and frequencies.

5.2 Spatial behavior and analytic equations

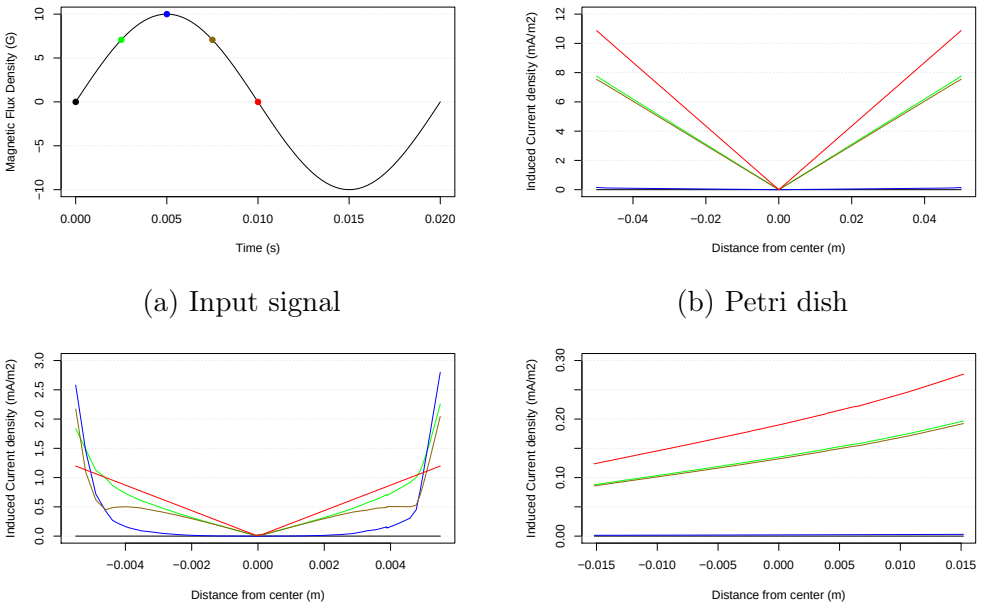

(a) Input signal

(b) Petri dish

(c) 48-well dish

(d) Tibia

Figure 34: Spatial distributions of induced current density in the models studied using 50Hz sinusoidal input. The temporal evolution of the distribution is plotted from five time points, shown in figure 34a as colored dots on the sine wave. The colors correspond to the colors of the lines in the plots b-d.

Figure 34 shows the spatial distributions of induced current densities on different plates on a line crossing the center point of each dish or bone. On the Petri dish, the spatial distribution follows the shape predicted by the analytical equation 21 of Bassen et al. at all time points. The maximum values arise at half wavelength -timepoint as expected from Faraday's law. The development of spatial distribution of the 48-well dish is already addressed at chapter 4.2.1, but at the half wavelength -time point it too follows the analytic equation 21.

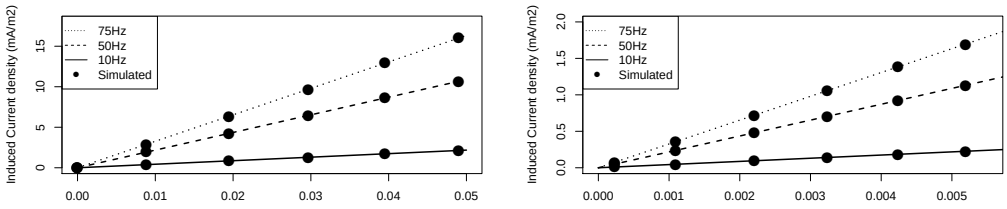

(a) Petri dish

(b) 48 well dish

Figure 35: Analytical and simulated current densities on Petri and 48-well dishes from center to the edge of the plate under exposure to sinusoidal magnetic fields.

The distribution predicted by equation 21 and distribution simulated on Petri and 48-well dishes are presented in figure 35. The maximal error between analytical and simulated solutions is 0.3% in all the cases compared.

The induced current densities were linearly dependent on radius of the dish as well as field frequency and amplitude also for triangular waves not discussed by Bassen et. all in their paper [42]. Based on the simulation result a novel equation 29 for an average cell culture medium with conductivity of 1.386 S/m was fitted to the data.

$$J = 0.277frB \tag{29}$$

In this equation, J is the induced current density in $\mathrm{mA/m^2}$, r is the radius of the disk in m, f is the frequency in Hz and B the amplitude of the external magnetic field in G. Figure 36 presents the spatial distribution of induced current densities on Petri and 48-well dishes with different amplitudes and frequencies alongside with the simulated data points. The maximal error between simulated data points and results from equation 29 is 0.7%.

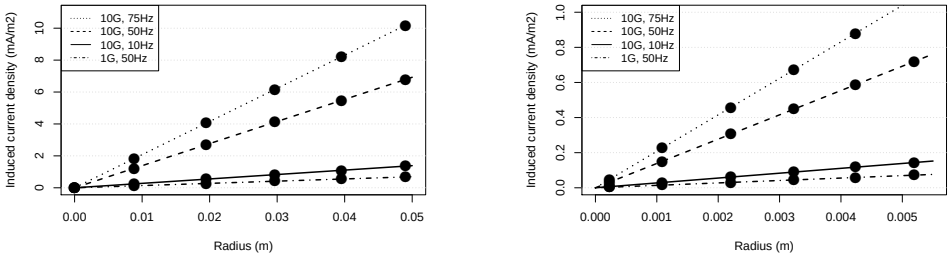

(a) Petri dish (b) 48 well dish

Figure 36: Analytical (lines) and simulated (points) current densities on Petri dish and 48-well dish models from center to the edge of the plate under exposure to triangular magnetic fields.

In similar manner a novel equation (30) can also be fitted for the average CCM exposed to square waved magnetic fields taking into account the independence from frequency and dependence on risetime t_{rise}.

$$J = 260Br/t_{rise} \tag{30}$$

This equation predicts the induced current densities of the simulations with maximal error of 1.75%. Figure 37 presents the induced current densities predicted by equation 30 alongside the simulated values.

On tibia and fibula the spatial distributions of induced fields are similar, having larger values closer to edge of the leg and smaller closer to the center. The induced fields are strongly affected by the currents flowing in more conductive muscle tissue around them. This effect can be seen from figure 38, which presents the induced current densities on a cross section of the leg model.

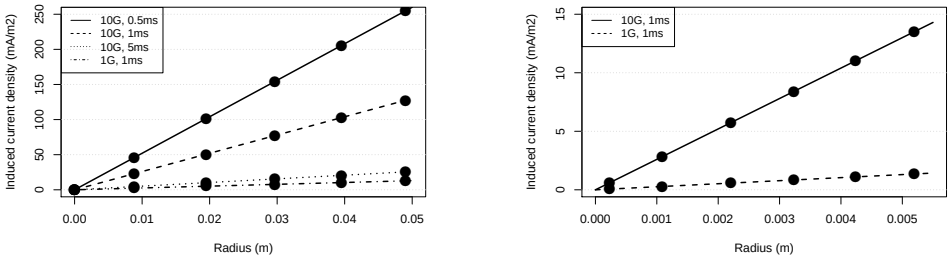

(a) Petri dish

(b) 48 well dish

Figure 37: Analytical (lines) and simulated (points) current densities on Petri dish and 48-well dish models from center to the edge of the plate under exposure to square waved magnetic fields.

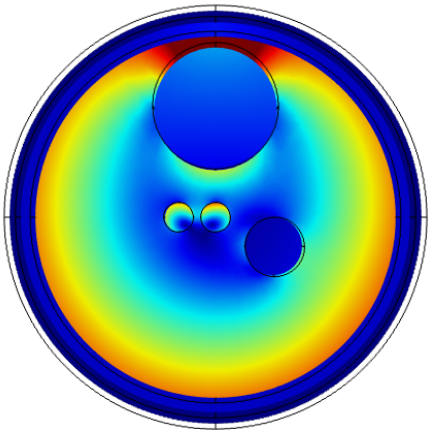

Figure 38: Induced current density distribution on a cross section of the leg model.

The spatial distribution of the induced fields in the muscle are similar to the Petri dish model although clearly disturbed by the two large veins and two bones modeled within it. Especially the thin gap modeled between Tibia and adipose tissue concentrates the currents raising the induced current density at this point most probably unrealistically high as there is no muscle between Tibia and adipose tissue at this point. This simplification was made in order to avoid problems in the numerical solver and it causes some inaccuracy to the spatial distribution of induced fields within tibia.

5.3 Orientation of the magnetic field

Figure 39 presents a comparison of 10-based logarithms of induced current densities of three different Petri dish orientations in external magnetic fields of 50 Hz and 10 G. As can be seen from the figure, for all the waveforms maximal induction occurs when Petri dish is placed perpendicular to the external field and minimal induction when the dish is parallel to the field. If the orientation is tilted 45 degrees, the amplitude of induced field is near the one of perpendicular orientation as the perpendicular component of the external field dominates the induced currents.

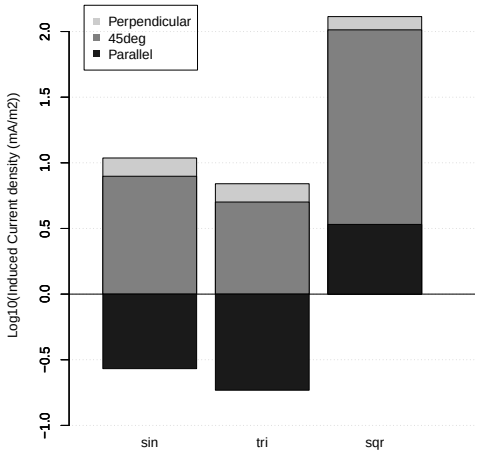

Figure 39: 10-based logarithms of induced current density on Petri dish at three orientations and waveforms.

Figure 40 presents the spatial distributions of induced current densities on Petri dish for the three orientations under the scope. When the Petri dish is oriented perpendicular to the external field, the induced field exhibits a strong dependence on the radius of the dish whereas in parallel orientation, the induced field along the x-axis is stable along the diameter of the Petri dish, variation being less than 2% for all waveforms, the line aside from transients at the edges of the dish. If the dish is tilted 45 degrees to the external field, the amplitude of induced field on the dish is smaller than with the perpendicular field the shape of the distribution is dominated by the perpendicular component of the field. The induced current density in the 45 degree orientation equates approximately the sum of the amplitudes of perpendicular and parallel amplitudes both divided by square root of two.

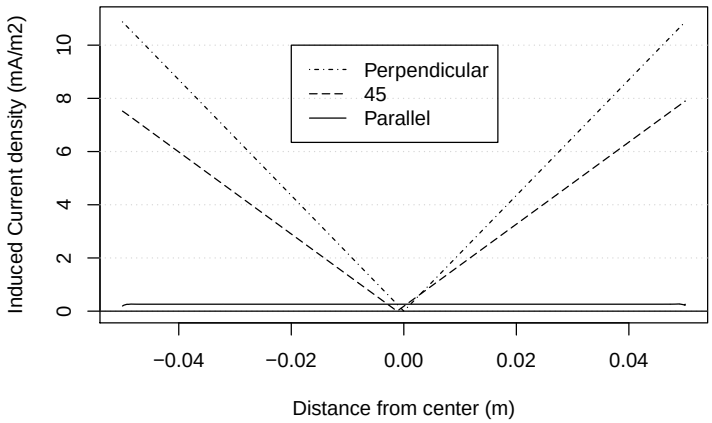

Figure 40: Spatial distribution of induced current density on Petri dish with three magnetic field orientations.

Table 16 presents the numerical values for results in figures 39.

	Parallel	45deg	Perpendicular
Sin	0.271	7.900	10.885
Tri	0.185	5.028	6.929
Sqr	3.395	103.003	129.939

Table 16: Induced current density maximums [mA/m^2] at different magnetic field waveforms at Petri dish, with three magnetic field orientations.

5.4 Volume of the cell culture medium

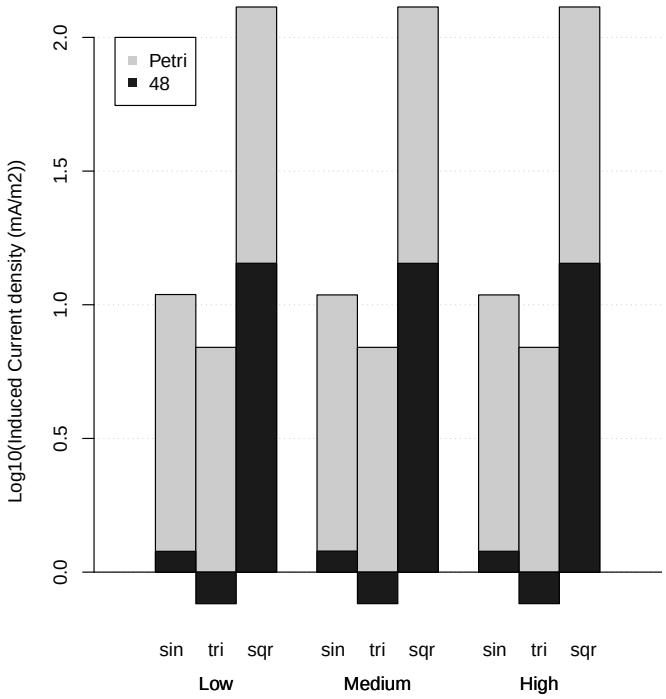

Figure 41: 10-based logarithms of maximal amplitudes of induced fields on three volumes of liquid in Petri dish and in 48-well dish within 10 G external magnetic field of three different shapes perpendicular to the dish. For Petri dish model Low=5 ml, Medium=10 ml and High=15 ml. For 48-well dish Low=0.1 ml, Medium=0.2 ml and High=0.5 ml.

Figure 41 represents a comparison of the effects of varying volume of the cell culture medium on a cell culture dish exposed to external magnetic field perpendicular to the dish. In the simulations, three volumes for both Petri dish (5, 10, 15 ml) and 48-well dish (0.1, 0.2, 0.5 ml) models were exposed to three waveforms of 10 G magnetic field. As can be seen from the data in this figure, the fields induced to circular dishes perpendicular to the external magnetic field are not sensitive to the volume of liquid on the dish on any of the tested waveforms. The highest difference between induced current densities of two volumes on any given waveform is 0.33%.

This does not apply in the case in which the dish is parallel to the external field as demonstrated in figure 42, which compares the parallel and perpendicular orientations on different volumes in terms of induced current densities. As can be seen from this figure, the induced fields exhibit a strong dependence on the amount of liquid on the plate parallel to the magnetic as the growing volume also creates a larger surface area exposed perpendicular to the external field.

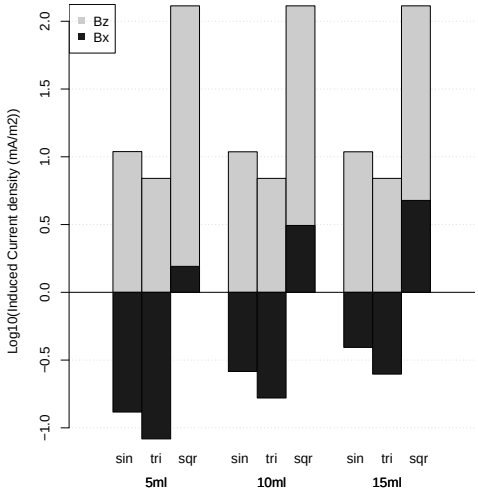

Figure 42: 10-based logarithms of maximal amplitudes of induced fields on three volumes of liquid in Petri dish within 10 G external magnetic field of three different shapes perpendicular and parallel to the dish.

Table 17 presents the numerical values for results in figures 41 and 42.

		Petri dish		
		5ml	10ml	15 ml
Parallel	Sin	0.131	0.261	0.392
	Tri	0.093	0.166	0.249
	Sqr	1.554	3.114	4.765
Perpendicular	Sin	10.921	10.885	10.885
	Tri	6.930	6.930	6.930
	Sqr	129.935	129.939	129.958

		48-well dish		
		0.1 ml	0.2 ml	0.5ml
Perpendicular	Sin	1.196	1.199	1.197
	Tri	0.761	0.762	0.762
	Sqr	14.298	14.290	14.291

Table 17: Induced current density maximums at different volumes of CCM at Petri dish and 48-well dish, with two different magnetic field orientations.

5.5 Thermal simulations

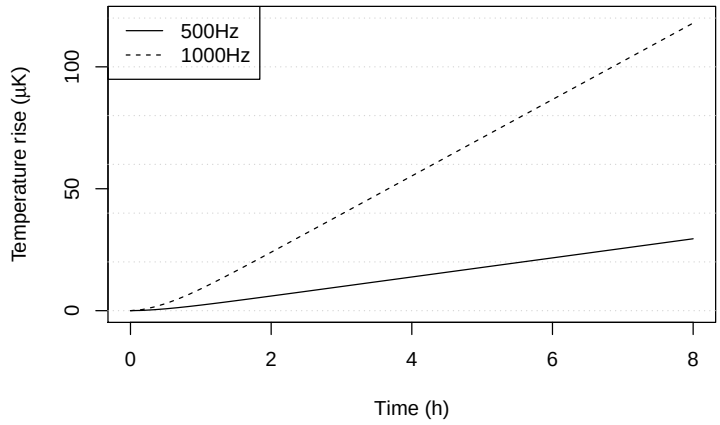

Figure 43: Temperature on the dish as a function of time at different frequencies when Petri dish is exposed to 10 G sinusoidal magnetic field.

Figure 43 represents the temperature of a Petri dish exposed to 10 G sinusoidal magnetic field perpendicular to the dish as a function of time. As can be seen from this figure, even higher frequencies than the ELF-range fail to elicit any significant change in the temperature of the cell culture medium. Table 18 presents the numerical values for results in figure 43.

	0h	1h	2h	3h	4h	5h	6h	7h	8h
500Hz	0	2	6	10	14	18	22	26	29
1000Hz	0	9	24	40	55	71	87	102	118

Table 18: Temperature rise in μK simulated at different timepoints. Temperature at time 0 is 310.15K

6 Discussion

Chapter 5 presented the results from Comsol simulations of a Petri dish, 48-well dish and a simplified model leg exposed to an external magnetic field with different parameters. Based on these results, it is clear that results obtained with different parameters should not be compared with each other. This is because, although small, most of the simulated maximum amplitudes of induced current densities on cell culture dishes studied reach the biological range (1-1000 mA/m^2) and the Bone growth signal on Petri dish managed even to exceed the upper limit. Only waveforms failing to reach the limit of 1 mA/m^2 were 10 Hz sinusoidal EMF and triangular EMFs of 10 Hz and 50 Hz. Therefore the idea of the induced fields affecting the cells on a cell culture dish should not be left out of consideration in ELF EMF studies although it has been argued in literature that the low amplitude ELF EMF would not induce fields that are capable of affecting tissue.

The cell samples in vitro are often prepared on different cell culture vessels depending on the assay. As there are great differences between the fields induced on different sized cell culture dishes, it is advised to expose the cells to a magnetic field on a single type of a dish or adjust the parameters to match the exposure between different cell culture vessels if multiple assays are needed. In case of exposing each set of cells on different kinds of cell culture dishes, the cells are exposed to different induced fields and the results might not be comparable with each other.

The amplitudes of the induced fields excited by sinusoidal EMFs were also found to be in correspondence with the analytic equation 21 as shown in figures 33 and 35. Based on the good match between analytical equation and simulated results, equation 21 the simulations of this thesis are correct and both the simulations and the analytic equation can be used to solve induced fields in Petri dish and also in multi-welled dishes. Bassen's equation can be generalized also to multi-welled dishes as the simulation results did not exhibit any capacitive effects in the ELF EMF range.

Interestingly, also triangular EMFs exhibited linear correspondence with both the amplitude, radius and the frequency of the external magnetic field. Furthermore the square waved EMFs were directly proportional to amplitude and radius and inversely proportional to the risetime of the square wave. Based on the maximum amplitudes simulated, analytic equations were fitted to simulation data in order to approximate the spatial distribution of fields induced by triangular and square waved magnetic field. These equations can be used to approximate exposure to induced fields between round cell culture dishes of various sizes containing an average CCM with a conductivity of 1.386 S/m exposed to triangular and square waved magnetic fields, although experimental data is still needed in order to asses the exact accuracy and validate these two equations.

The radial dependence on the round cell culture dishes in general is an interesting phenomena as it results in inhomogeneous exposure of cells to the induced fields

even within an uniform external magnetic field. Based on the simulation results, an experiment could be designed to expose a cell culture dish to such an external magnetic field that the resulting current density distribution would be uniform on the cell culture dish. This would answer the question, whether the non-uniformity affects the cells on a round cell culture dish. This could for example be achieved using a high magnetic field amplitude parallel to the cell culture vessel since parallel orientation was shown to result in uniform distribution of induced fields as will be discussed shortly.

Yet another noteworthy aspect on the maximum amplitudes induced is the independence of induced current density of the frequency of external square-waved magnetic field. Instead, the amplitude of the induced field is inversely proportional to the rise time of the square wave as presented in figure 32. Although this results directly from Faraday's law, it is rarely considered in literature. This is exceptional as it clearly has a strong impact on the induced fields.

As was shown in figure 30, the temporal behavior of different waveforms can be divided into different categories based on the form of stimulating external magnetic field. Sinusoidal input results in sinusoidal output, triangular input in square-like output and square input in transient like behavior. Again these results can be expected from Faraday's law but are seldom discussed in literature. On a given external magnetic field intensity, triangular waves exhibited the largest area under the curve and square waves give highest induced current densities. The lowest induced current density and area under the curve were excited by triangular magnetic field and bone signal, respectively. Based on the AUCs and maximal amplitudes of induced current densities by sinusoidal and triangular magnetic fields, there seems not to be much difference in the induced fields by these signals. Yet, as it is unknown whether the induced fields are capable of eliciting biological response, the difference in the magnetic field shapes cannot be omitted from experiments. Together the combined effect of peak amplitude and differing area under the curve could explain to some extent why the results of in vitro experiments are inconsistent. Some cellular functions like the action potentials can be triggered by a short high amplitude current pulse, whereas some functions like the cell migration benefit from a long lasting stable currents.

The results on temporal behavior raise also a question on the symmetry of the induced fields. A symmetrical external field lead to symmetrical induced field and thus vibrating currents on the cell culture dish. Adding some asymmetry to the external magnetic field waveform could have a beneficial effect on migration for example, as the induced fields would last longer in some directions than others.

The effect of orientation of the external magnetic field was also studied. Based on these results, the perpendicular orientation is found to exhibit the highest induced fields and parallel orientation the lowest. Also the spatial distributions of induced fields between these two orientations differs strongly: the perpendicular orientation

exhibits a dependence on the radius according to equation 21 whereas in the parallel orientation the radial distribution stays stable along the radial line except for a transient at the side. For the 45 degree case, both the spatial distribution and amplitude of the induced field are dominated by the perpendicular component of the magnetic field. The amplitude of induced current density is approximately the sum of perpendicular and parallel induced fields when both are divided by the square root of two. The perpendicular orientation was also found to be independent of the volume of the liquid where as the parallel orientation results in linear dependence of the volume on the dish as suggested by Bassen et al.

Based on these results, it is suggested not to directly compare the results from studies if the orientation of the magnetic fields differ, as the induced currents vary vastly and only the square waved signals reach the biological limits in parallel orientation. As the experiments are often conducted in parallel orientation and the amounts of cell culture medium used on the cell culture dishes are not usually reported, care should be taken when comparing results even with apparently similar studies conducted in the parallel orientation.

It should also be noted, that even the resulted maximum amplitudes that are below the biological range are still rather close to it. This raises the question, whether it is possible even for these lower currents to enhance the ongoing endogenous currents through summation and therefore also affect the biological phenomena regulated by the currents. This boost effect can also be present with the current densities reaching the lower end of the biological range, such as the currents induced to the Petri and 48-well dishes with sinusoidal and triangular inputs. As a high current density spike that lowers down after a while in bone fractures has been reported, it could be argued that it is possible for a square waves to induce high enough a current density in a bone to restart a non-union bone fracture based on the approximately 100 $\mathrm{mA/m^2}$ simulated in Tibia with bone growth signal.

When the simulated values at the bones and cell culture dishes are compared, the induced fields on the cell culture dishes are found to be up to 40 times larger than corresponding values at the bones. This would suggest that based solely on the induced fields, the cell culture dishes would over estimate the induced fields. Yet, as is the case with non-union fractures for example, in vivo the tissue is often exposed to ELF magnetic fields in order to treat something that has been damaged. As multiple tissues as well as intra- and extracellular fluids have higher conductivity than the intact bone tissue, it is possible that the simulations used here in fact underestimate the conductivity of the damaged tissue, where the material properties differ from the intact tissue. Thereby also the induced fields induced would be larger than the ones simulated. More elaborate models and measurements of conductivities at damaged tissues would be needed in order to fully evaluate the representativeness of in vitro studies.

In the thermal simulations, no significant heating of the cell culture medium was

observed, even though the heat exchange with surroundings is not considered in the simulations. This supports the notion in table 3 suggesting the ELF EMFs to contain too little energy to cause heating in tissues. The maximum simulated temperature rise of 118 μK resulted with 1 kHz frequency after 8 hours of exposure to sinusoidal EMF. As the Petri dish exhibited the highest induced fields of the setups tested, it can be assumed that the heating caused by low amplitude ELF EMF in 48-well dish or within the leg is even less significant than it is within the Petri dish.

The parametric behavior of fields induced by ELF EMF have been studied in this thesis in order to get new insight for designing in vitro experiments in a meaningful way. Although the induced current density is used to describe the results of the simulations, it is still unknown whether induced currents can affect the functions of cells. By using the results of this thesis, it is possible to design in vitro experiments in such a way, that the induced fields on Petri dish and 48-well dish are identical. This setup opens the possibility to asses whether the similar induced fields results in similar effects on cells or does varying the magnetic field control the interaction. To find out the dominant phenomenon, one set of experiments with identical magnetic fields and another with identical induced fields for the two cell culture dishes of different sizes can be used. In the case that induced field proves to be more dominant, the different magnetic waveforms exciting identical spatial induced field distribution can be used to stimulate cells in order to asses the effect of waveform on cells accurately. Such an experiment could give valuable information on how parameters affect the outcome of an ELF EMF stimulation of cells.

There are many topics on this subject still needing further research. As the results of this thesis are solely based on simulation, experimental data is needed to validate the results. Also, only a scarce portion of different cell culture dishes was modeled in this thesis. It would be interesting to find out how does the shape of the cell culture dishes affect the induced fields. For example chamber slides and other non-round cell culture dishes could be easily modeled with Comsol Multiphysics. Experimental-wise, these results open interesting new possibilities to be studied in order get more understanding in the coupling of ELF EMF and biological tissue.

7 Conclusions

Models of two cell culture dishes and a simplified model of a leg were built for this thesis and in total 89 Comsol simulations were run in order to obtain new insight into low amplitude ELF EMF dosimetry and on effects of different magnetic field parameters on the induced fields.

Based on the simulation results, the radius and orientation to the external magnetic field of the cell culture dish as well as the waveform, amplitude, frequency of the external magnetic field were found to be important parameters regarding the induced fields. It is therefore suggested that they should be taken into consideration when planning an in vitro experiment. Although sinusoidal and triangular waves result in similar amplitudes and AUCs it cannot be ruled out based on simulations alone that the different temporal behavior of the signals would not affect cells in different manner. Induced field amplitudes by square waved magnetic fields were found to be independent of the frequency of the magnetic field but instead dependent on the rise time of the magnetic field. Based on this, it suggested that the rise time should always be mentioned when reporting rectangular wave ELF EMF study methods.

This thesis proposes novel equations for approximating the fields induced by triangular and square waved magnetic fields on a circular cell culture dish. Together with the equation of Bassen, these three equations create a usable tool to quickly design and optimize the dosimetry for in vitro ELF EMF experiments. The proposed equations will need experimental validation. The measurement of induced currents within an external magnetic is out of the scope for this thesis, due to the difficulty of avoiding interference between the measurement probe and the magnetic field.

The induced current densities on the cell culture dishes were found to lie in the lower end or just below the biological range when sinusoidal and triangular waveforms were used. With square waves, higher current densities can be obtained on both dishes. The induced fields with all parameters were higher than the ones simulated at the bones of the leg model suggesting that the fields induced in vitro overestimate the fields induced in vivo to an unharmed bone tissue. This overestimation can be easily taken into account when planning an in vitro experiment by adjusting the amplitude of the magnetic field or simply by using smaller cell culture dishes.

The review and simulations conducted for this thesis suggest that the induced current densities vary greatly depending on exposure parameters and are capable of reaching the endogenous range of biological fields. Therefore careful parameter consideration cannot be omitted when planning of an in vitro experiment. This thesis offers tools for planning in vitro experiments in a physically meaningful way to provide new insight into the biological effects of ELF EMF.

References

[1] D. J. Griffiths, "Introduction to electrodynamics," *Pearson Education, Inc.*, 2008.

[2] H. Nyberg and K. Jokela, "Sähkomagneettiset kentät," *Säteilyturvakeskus*, 2006.

[3] M. Mansfield and C. O'Sullivan, "Understanding physics," *John Wiley & Sons*, 2008.

[4] https://skullsinthestars.files.wordpress.com/2009/04/diamagnet.jpg, 20.7.2015.

[5] E. Kaniusas, "Biomedical sensors and signals I," *Springer*, 2012.

[6] http://www.easynotecards.com/uploads/976/88/_4a88b4c5_140c98ff4b1_ _8000_00005336.jpg, 20.7.2015.

[7] G. Tortora and B. Derrickson, "Principles of anatomy and physiology," *John Wiley & Sons*, 2009.

[8] https://upload.wikimedia.org/wikipedia/commons/4/4f/Sodium-potassium_ pump_and_diffusion.png, 20.7.2015.

[9] B. Alberts, A. Johnson, J. Lewis, M. Raff, K. Roberts, and P. Walter, "Molecular biology of the cell," *Garland Science*, 2008.

[10] N. Shcheynikov, A. Son, J. H. Hong, O. Yamazaki, E. Ohana, I. Kurtz, D. M. Shin, and S. Muallem, "Intracellular Cl- as a signaling ion that potently regulates Na+/HCO3-transporters," *Proceedings of the National Academy of Sciences*, vol. 112, no. 3, pp. E329–E337, 2015.

[11] R. Nuccitelli, "Endogenous ionic currents and DC electric fields in multicellular animal tissues," *Bioelectromagnetics*, vol. 13, no. S1, pp. 147–157, 1992.

[12] G. Luxardi, B. Reid, P. Maillard, and M. Zhao, "Single cell wound generates electric current circuit and cell membrane potential variations that requires calcium influx," *Integr. Biol.*, vol. 6, pp. 662–672, 2014.

[13] M. Zhao, "Electrical fields in wound healing - an overriding signal that directs cell migration," *Seminars in Cell & Developmental Biology*, vol. 20, no. 6, pp. 674 – 682, 2009.

[14] F. Chang and N. Minc, "Electrochemical control of cell and tissue polarity," *Annual Review of Cell and Developmental Biology*, vol. 30, no. 1, pp. 317–336, 2014.

[15] M. Levin, "Large-scale biophysics: ion flows and regeneration," *Trends in Cell Biology*, vol. 17, no. 6, pp. 261 – 270, 2007.

[16] http://site.motifolio.com/images/Passive-and-active-fluxes-maintain-the-resting-membrane-potential 5111223.png, 20.7.2015.

[17] S. Groppa, A. Oliviero, A. Eisen, A. Quartarone, L. Cohen, V. Mall, A. Kaelin-Lang, T. Mima, S. Rossi, G. Thickbroom, P. Rossini, U. Ziemann, J. Valls-Sola, and H. Siebner, "A practical guide to diagnostic transcranial magnetic stimulation: Report of an {IFCN} committee," *Clinical Neurophysiology*, vol. 123, no. 5, pp. 858 – 882, 2012.

[18] M. Mansfield and C. O'Sullivan, "Environmental health criteria 238: Extremely low frequency fields," *World Health Organization*, 2007.

[19] R. H. Funk, T. Monsees, and N. Azkukur, "Electromagnetic effects - from cell biology to medicine," *Progress in Histochemistry and Cytochemistry*, vol. 43, no. 4, pp. 177 – 264, 2009.

[20] P. A. Valberg, R. Kavet, and C. N. Rafferty, "Can low-level 50/60 Hz electric and magnetic fields cause biological effects?" *Radiation Research*, vol. 148, no. 1, pp. 2–21, 1997.

[21] D. Formica and S. Silvestri, "Biological effects of exposure to magnetic resonance imaging: an overview." *BioMedical Engineering Online*, vol. 3, pp. 11 – 12, 2004.

[22] S. Gabriel, R. W. Lau, and C. Gabriel, "The dielectric properties of biological tissues: II. Measurements in the frequency range 10 Hz to 20 GHz," *Physics in Medicine and Biology*, vol. 41, no. 11, p. 2251, 1996.

[23] S. Iivonen, "Models and methods for computational electromagnetic dosimetry," Ph.D. dissertation, Helsinki University of Technology, 2009.

[24] https://en.wikipedia.org/wiki/Properties_of_water, 23.7.2015.

[25] C. G. Malmberg and A. A. Maryott, "Dielectric constant of water from 0 to 100 C," *Journal of Research of the National Bureau of Standards*, vol. 56, no. 1, 1956.

[26] W. M. Spees, D. A. Yablonskiy, M. C. Oswood, and J. J. Ackerman, "Water proton mr properties of human blood at 1.5 tesla: Magnetic susceptibility, T1, T2, T*2, and non-lorentzian signal behavior," *Magnetic Resonance in Medicine*, vol. 45, no. 4, pp. 533–542, 2001.

[27] S. Gabriel, R. W. Lau, and C. Gabriel, "The dielectric properties of biological tissues: III. Parametric models for the dielectric spectrum of tissues," *Physics in Medicine and Biology*, vol. 41, no. 11, p. 2271, 1996.

[28] http://www.fda.gov/MedicalDevices/ProductsandMedicalProcedures/DeviceApprovalsandClearances/Recently-ApprovedDevices/ucm125520.htm, 23.7.2015.

[29] A. K. Compton, B. Shah, and S. M. Hayek, "Spinal cord stimulation: A review," *Current Pain and Headache Reports*, vol. 16, no. 1, pp. 35–42, 2012.

[30] H. Beck, W. E. Boden, S. Patibandla, D. Kireyev, V. Gupta, F. Campagna, M. E. Cain, and J. E. Marine, "50th anniversary of the first successful permanent pacemaker implantation in the united states: Historical review and future directions," *The American Journal of Cardiology*, vol. 106, no. 6, pp. 810 – 818, 2010.

[31] K. Hug and M. Röösli, "Therapeutic effects of whole-body devices applying pulsed electromagnetic fields (PEMF): A systematic literature review," *Bioelectromagnetics*, vol. 33, no. 2, pp. 95–105, 2012.

[32] R. Kavet, M. A. Stuchly, W. H. Bailey, and T. D. Bracken, "Evaluation of biological effects, dosimetric models, and exposure assessment related to ELF electric- and magnetic-field guidelines," *Applied Occupational and Environmental Hygiene*, vol. 16, no. 12, pp. 1118–1138, 2001.

[33] C. Durney, "Electromagnetic dosimetry for models of humans and animals: A review of theoretical and numerical techniques," *Proceedings of the IEEE*, vol. 68, no. 1, pp. 33–40, Jan 1980.

[34] S. Caorsi, M. Pastorino, and M. Raffetto, "Analytic SAR computation in a multilayer elliptic cylinder for bioelectromagnetic applications," *Bioelectromagnetics*, vol. 20, no. 6, pp. 365–371, 1999.

[35] M. Caon, "Voxel-based computational models of real human anatomy: A review," *Radiation and Environmental Biophysics*, vol. 42, no. 4, pp. 229–235, 2004.

[36] J. Hwang, R. Shoup, G. Warner, and J. Poston, "Mathematical descriptions of a one- and five-year old child for use in dosimetry calculations," *Oak Ridge National Laboratory*, vol. Oak Ridge, TN, USA, 1976.

[37] A. Christ, W. Kainz, E. G. Hahn, K. Honegger, M. Zefferer, E. Neufeld, W. Rascher, R. Janka, W. Bautz, J. Chen, B. Kiefer, P. Schmitt, H.-P. Hollenbach, J. Shen, M. Oberle, D. Szczerba, A. Kam, J. W. Guag, and N. Kuster, "Virtual family - development of surface-based anatomical models of two adults and two children for dosimetric simulations," *Physics in Medicine and Biology*, vol. 55, no. 2, p. N23, 2010.

[38] "http://www.itis.ethz.ch/virtual-population/virtual-population-cvip-vip/vip2/," 1.8.2015.

[39] "http://www.itis.ethz.ch/virtual-population/virtual-population-cvip-vip/cvip3-and-vip1/," 1.8.2015.

[40] International Commission on non-ionizing radiation protection, "Icnirp guidelines for limiting exposure to time-varying electric and magnetic fields (1hz - 100khz)," *Healt Physics*, vol. 99, no. 6, pp. 818–836, 2010.

[41] http://ec.europa.eu/environment/chemicals/lab_animals/3r/alternative_en.htm, 27.7.2015.

[42] H. Bassen, T. Litovitz, M. Penafiel, and R. Meister, "ELF in vitro exposure systems for inducing uniform electric and magnetic fields in cell culture media," *Bioelectromagnetics*, vol. 13, no. 3, pp. 183–198, 1992.

[43] M. Yamada, K. Tanemura, S. Okada, A. Iwanami, M. Nakamura, H. Mizuno, M. Ozawa, R. Ohyama-Goto, N. Kitamura, M. Kawano, K. Tan-Takeuchi, C. Ohtsuka, A. Miyawaki, A. Takashima, M. Ogawa, Y. Toyama, H. Okano, and T. Kondo, "Electrical stimulation modulates fate determination of differentiating embryonic stem cells," *Stem cells*, vol. 25, no. 3, pp. 562–570, 2007.

[44] G. Cheng, Y. Zhai, K. Chen, J. Zhou, G. Han, R. Zhu, L. Ming, P. Song, and J. Wang, "Sinusoidal electromagnetic field stimulates rat osteoblast differentiation and maturation via activation of NO–cGMP–PKG pathway," *Nitric Oxide*, vol. 25, no. 3, pp. 316–325, 2011.

[45] M.-T. Tsai, W.-J. Li, R. S. Tuan, and W. H. Chang, "Modulation of osteogenesis in human mesenchymal stem cells by specific pulsed electromagnetic field stimulation," *Journal of orthopaedic research: official publication of the Orthopaedic Research Society*, vol. 27, no. 9, p. 1169, 2009.

[46] J. Zhou, J.-Q. Wang, B.-F. Ge, X.-N. Ma, H.-P. Ma, C. J. Xian, and K.-M. Chen, "Different electromagnetic field waveforms have different effects on proliferation, differentiation and mineralization of osteoblasts in vitro," *Bioelectromagnetics*, vol. 35, no. 1, pp. 30–38, 2014.

[47] A. C. Polycarpou, "Introduction to the finite element method in electromagnetics," *Synthesis Lectures on Computational Electromagnetics*, vol. 1, no. 1, pp. 1–126, 2005.

[48] http://www.goodfellow.com/E/Polystyrene.html, 27.7.2015.

[49] X. Jin, Y. Zhao, A. Richardson, L. Moore, P. S. Williams, M. Zborowski, and J. J. Chalmers, "Differences in magnetically induced motion of diamagnetic, paramagnetic, and superparamagnetic microparticles detected by cell tracking velocimetry," *The Analyst*, vol. 133, no. 12, pp. 1767–1775, 2008.

[50] http://www.thermoscientific.com/en/product/nunc-petri-dishes.html, 27.7.2015.

[51] http://etc.usf.edu/clipart/52800/52879/52879_leg_lg.gif, 27.7.2015.

[52] R. Pethig, "Dielectric properties of body tissues," *Clinical Physics and Physiological Measurement*, vol. 8, no. 4A, p. 5, 1987.

[53] Z. Chen, J. Ellis, and E. D. Dahlberg, "A simple technique to measure the magnetic susceptibility of liquids," *Review of Scientific Instruments*, vol. 83, no. 9, pp. –, 2012.

[54] I. Martinez, "Properties of some particular solutions," *Universidad Politecnica de Madrid*, 2015.

[55] *Material Library of COMSOL Multiphysics 5.0.*

[56] C. Gabriel, S. Gabriel, and E. Corthout, "The dielectric properties of biological tissues: I. Literature survey," *Physics in Medicine and Biology*, vol. 41, no. 11, p. 2231, 1996.

[57] H.-W. Huang, C.-T. Liauh, C.-Y. Chou, T.-C. Shih, and W.-L. Lin, "A fast adaptive power scheme based on temperature distribution and convergence value for optimal hyperthermia treatment," *Applied Thermal Engineering*, vol. 37, no. 0, pp. 103 – 111, 2012.

[58] D. L. Ingram, "Evaporative cooling in the pig," *Nature*, vol. 207, pp. 45–416, 1965.

[59] V. D. Santis, X. L. Chen, I. Laakso, and A. Hirata, "An equivalent skin conductivity model for low-frequency magnetic field dosimetry," *Biomedical Physics & Engineering Express*, vol. 1, no. 1, p. 015201, 2015.

[60] J.-E. Park, Y.-K. Seo, H.-H. Yoon, C.-W. Kim, J.-K. Park, and S. Jeon, "Electromagnetic fields induce neural differentiation of human bone marrow derived mesenchymal stem cells via ros mediated egfr activation," *Neurochemistry international*, vol. 62, no. 4, pp. 418–424, 2013.

[61] C. Grassi, M. D'Ascenzo, A. Torsello, G. Martinotti, F. Wolf, A. Cittadini, and G. B. Azzena, "Effects of 50Hz electromagnetic fields on voltage-gated Ca2+ channels and their role in modulation of neuroendocrine cell proliferation and death," *Cell Calcium*, vol. 35, no. 4, pp. 307–315, 2004.

[62] J. Chen, L.-Q. Huang, Q.-J. Xia, and C.-Q. He, "Effects of pulsed electromagnetic fields on the mRNA expression of CAII and RANK in ovariectomized rats," *Rheumatology international*, vol. 32, no. 6, pp. 1527–1532, 2012.

[63] W. H.-S. Chang, L.-T. Chen, J.-S. Sun, and F.-H. Lin, "Effect of pulse-burst electromagnetic field stimulation on osteoblast cell activities," *Bioelectromagnetics*, vol. 25, no. 6, pp. 457–465, 2004.

[64] G. Hannay, D. Leavesley, and M. Pearcy, "Timing of pulsed electromagnetic field stimulation does not affect the promotion of bone cell development," *Bioelectromagnetics*, vol. 26, no. 8, pp. 670–676, 2005.

[65] J. W. Kronberg, "Digital electronic bone growth stimulator," Patent: US541596 A, 9.5.1995.

[66] F. Luo, T. Hou, Z. Zhang, Z. Xie, X. Wu, and J. Xu, "Effects of pulsed electromagnetic field frequencies on the osteogenic differentiation of human mesenchymal stem cells," *Orthopedics*, vol. 35, no. 4, p. 282, 2012.

[67] X. Zhang, X. Liu, L. Pan, and I. Lee, "Magnetic fields at extremely low-frequency (50Hz, 0.8 mT) can induce the uptake of intracellular calcium levels in osteoblasts," *Biochemical and biophysical research communications*, vol. 396, no. 3, pp. 662–666, 2010.

[68] M. T. Santini, G. Rainaldi, A. Ferrante, P. L. Indovina, P. Vecchia, and G. Donelli, "Effects of a 50 Hz sinusoidal magnetic field on cell adhesion molecule expression in two human osteosarcoma cell lines (mg-63 and saos-2)," *Bioelectromagnetics*, vol. 24, no. 5, pp. 327–338, 2003.

[69] L.-Y. Sun, D.-K. Hsieh, T.-C. Yu, H.-T. Chiu, S.-F. Lu, G.-H. Luo, T. K. Kuo, O. K. Lee, and T.-W. Chiou, "Effect of pulsed electromagnetic field on the proliferation and differentiation potential of human bone marrow mesenchymal stem cells," *Bioelectromagnetics*, vol. 30, no. 4, pp. 251–260, 2009.

[70] M. Markov, "Pulsed electromagnetic field therapy history, state of the art and future," *The Environmentalist*, vol. 27, no. 4, pp. 465–475, 2007.

[71] G. A. Gordon, "Designed electromagnetic pulsed therapy: Clinical applications," *Journal of Cellular Physiology*, vol. 212, no. 3, pp. 579–582, 2012.

[72] "Iron sphere in a 60 Hz magnetic field," *Comsol application gallery*, vol. Application ID: 12841, 2015.

A List of simulations

This appendix lists the simulations conducted for this thesis and their parameters.

	Waveform	Model	B(G)	f(Hz)	μ	σ (S/m)	ϵ	Mesh
1	Sin	Petri	10	50	1-1.11e^{-5}	1.386	75	1layer, Normal
2	Sin	Petri	10	50	1-1.11e^{-5}	1.386	75	2layer, Normal
3	Sin	Petri	10	50	1-1.11e^{-5}	1.386	75	3layer, Normal
4	Sin	Petri	10	50	1-1.11e^{-5}	1.386	75	4layer, Normal
5	Sin	48	10	50	1-1.11e^{-5}	1.386	75	1layer, Normal
6	Sin	48	10	50	1-1.11e^{-5}	1.386	75	2layer, Normal
7	Sin	48	10	50	1-1.11e^{-5}	1.386	75	3layer, Normal
8	Sin	48	10	50	1-1.11e^{-5}	1.386	75	4layer, Normal
9	Sin	1well	10	50	1-1.11e^{-5}	1.386	75	3layer, fine
10	Sin	1well	10	50	1-1.11e^{-5}	1.386	75	4layer, extra fine
11	Sin	Leg	10	50	1-1.11e^{-5}	1.386	75	Extra coarse
12	Sin	Leg	10	50	1-1.11e^{-5}	1.386	75	Coarse
13	Sin	Leg	10	50	1-1.11e^{-5}	1.386	75	Fine
14	Sin	Leg	10	50	1-1.11e^{-5}	1.386	75	Extra fine
15	Sin	Petri	10	50	0.9	1.5	75	3layer, Normal
16	Sin	Petri	10	50	1	1.5	75	3layer, Normal
17	Sin	Petri	10	50	1.1	1.5	75	3layer, Normal
18	Sin	Petri	10	50	1	1	75	3layer, Normal
19	Sin	Petri	10	50	1	2	75	3layer, Normal
20	Sin	Petri	10	50	1	1.5	25	3layer, Normal
21	Sin	Petri	10	50	1	1.5	$8e^7$	3layer, Normal

Table A1: Magnetic field (mf) simulations made for tuning the model.

	Type	Waveform	Model	B(G)	f(Hz)	V(ml)	Orientation	Risetime (ms)
22	ht	sin	Petri	10	500	10	$\perp$	-
23	ht	sin	Petri	10	1000	10	$\perp$	-

Table A2: Thermal simulations

	Type	Waveform	Model	B(G)	f(Hz)	V(ml)	Orientation	Risetime (ms)
24	mf	Sin	Petri	10G	10Hz	10	⊥	-
25	mf	Sin	Petri	10G	50Hz	10	⊥	-
26	mf	Sin	Petri	10G	75Hz	10	⊥	-
27	mf	Sin	48	10G	10Hz	0.2	⊥	-
28	mf	Sin	48	10G	50Hz	0.2	⊥	-
29	mf	Sin	48	10G	75Hz	0.2	⊥	-
30	mf	Sin	Leg	10G	10Hz	-	⊥	-
31	mf	Sin	Leg	10G	50Hz	-	⊥	-
32	mf	Sin	Leg	10G	75Hz	-	⊥	-
33	mf	Tri	Petri	10G	10Hz	10	⊥	-
34	mf	Tri	Petri	10G	50Hz	10	⊥	-
35	mf	Tri	Petri	10G	75Hz	10	⊥	-
36	mf	Tri	48	10G	10Hz	0.2	⊥	-
37	mf	Tri	48	10G	50Hz	0.2	⊥	-
38	mf	Tri	48	10G	75Hz	0.2	⊥	-
39	mf	Tri	Leg	10G	10Hz	-	⊥	-
40	mf	Tri	Leg	10G	50Hz	-	⊥	-
41	mf	Tri	Leg	10G	75Hz	-	⊥	-
42	mf	Sqr	Petri	10G	10Hz	10	⊥	1
43	mf	Sqr	Petri	10G	50Hz	10	⊥	1
44	mf	Sqr	Petri	10G	75Hz	10	⊥	1
45	mf	Sqr	48	10G	10Hz	0.2	⊥	1
46	mf	Sqr	48	10G	50Hz	0.2	⊥	1
47	mf	Sqr	48	10G	75Hz	0.2	⊥	1
48	mf	Sqr	Leg	10G	10Hz	-	⊥	1
49	mf	Sqr	Leg	10G	50Hz	-	⊥	1
50	mf	Sqr	Leg	10G	75Hz	-	⊥	1
51	mf	Sqr	Petri	10G	50Hz	10	⊥	0.5
52	mf	Sqr	Petri	10G	50Hz	10	⊥	3
53	mf	Sqr	Petri	10G	50Hz	10	⊥	5
54	mf	Bone	Petri	10G	-	10	⊥	0.01
55	mf	Bone	48	10G	-	0.2	⊥	0.01
56	mf	Bone	Leg	10G	-	-	⊥	0.01

Table A3: Simulations to compare different magnetic field parameters.

	Type	Waveform	Model	B(G)	f(Hz)	V(ml)	Orientation	Risetime (ms)
57	mf	Sin	Petri	1G	50Hz	10	$\perp$	-
58	mf	Sin	48	1G	50Hz	0.2	$\perp$	-
59	mf	Sin	Leg	1G	50Hz	-	$\perp$	-
60	mf	Tri	Petri	1G	50Hz	10	$\perp$	-
61	mf	Tri	48	1G	50Hz	0.2	$\perp$	-
62	mf	Tri	Leg	1G	50Hz	-	$\perp$	-
63	mf	Sqr	Petri	1G	50Hz	10	$\perp$	1
64	mf	Sqr	48	1G	50Hz	0.2	$\perp$	1
65	mf	Sqr	Leg	1G	50Hz	-	$\perp$	1
66	mf	Sin	Petri	10G	50Hz	10	45°	-
67	mf	Sin	Petri	10G	50Hz	10	$\parallel$	-
68	mf	Tri	Petri	10G	50Hz	10	45°	-
69	mf	Tri	Petri	10G	50Hz	10	$\parallel$	-
70	mf	Sqr	Petri	10G	50Hz	10	45°	-
71	mf	Sqr	Petri	10G	50Hz	10	$\parallel$	-
72	mf	Sin	Petri	10G	50Hz	5	$\perp$	-
73	mf	Sin	Petri	10G	50Hz	15	$\perp$	-
74	mf	Sin	Petri	10G	50Hz	5	$\parallel$	-
75	mf	Sin	Petri	10G	50Hz	15	$\parallel$	-
76	mf	Sin	48	10G	50Hz	0.1	$\perp$	-
77	mf	Sin	48	10G	50Hz	0.5	$\perp$	-
78	mf	Tri	Petri	10G	50Hz	5	$\perp$	-
79	mf	Tri	Petri	10G	50Hz	15	$\perp$	-
80	mf	Tri	Petri	10G	50Hz	5	$\parallel$	-
81	mf	Tri	Petri	10G	50Hz	15	$\parallel$	-
82	mf	Tri	48	10G	50Hz	0.1	$\perp$	-
83	mf	Tri	48	10G	50Hz	0.5	$\perp$	-
84	mf	Sqr	Petri	10G	50Hz	5	$\perp$	1
85	mf	Sqr	Petri	10G	50Hz	15	$\perp$	1
86	mf	Sqr	Petri	10G	50Hz	5	$\parallel$	1
87	mf	Sqr	Petri	10G	50Hz	15	$\parallel$	1
88	mf	Sqr	48	10G	50Hz	0.1	$\perp$	1
89	mf	Sqr	48	10G	50Hz	0.5	$\perp$	1

Table A4: Simulations to compare the amplitude and orientation of the magnetic field and the volume of the CCM.